The HadCM3 contribution to PlioMIP Phase 2.

Stephen J. Hunter[1], Alan M Haywood[1], Aisling M. Dolan[1], and Julia C. Tindall[1]

[1]University of Leeds, Leeds, LS2 9JT, UK

Correspondence to: Stephen J. Hunter (S.Hunter@leeds.ac.uk)

Abstract. We present the UK's input into the Pliocene Model Intercomparison Project Phase 2 (PlioMIP2) using the HadCM3 climate model. The 400 ppm CO_2 Pliocene experiment has a mean annual surface air temperature that is 2.9°C warmer than the pre-industrial and a polar amplification of between 1.7 and 2.2 times the global mean warming. The PRISM4 enhanced Pliocene palaeogeography accounts for a warming of 1.4°C whilst the CO_2 increase from 280 to 400 ppm leads to a further 1.5°C of warming. Climate sensitivity is 3.5°C for the pre-industrial and 2.9°C for the Pliocene. Precipitation change between the pre-industrial and Pliocene is complex, with geographic and land surface changes primarily modifying the geographical extent of mean annual precipitation. Sea ice fraction and areal extent is reduced during the Pliocene particularly in the southern hemisphere, although it persists through summer in both hemispheres. The Pliocene palaeogeography drives a more intense Pacific and Atlantic Meridional Overturning Circulation (AMOC). This intensification of AMOC is coincident with more widespread deep convection in the Southern Ocean and North Atlantic. We conclude by examining additional sensitivity experiments and confirm that the choice of total solar insolation (1361 vs. 1365 Wm^{-2}) and orbital configuration (modern vs. 3.205 Ma) do not significantly influence the anomaly-type analysis in use by the Pliocene community.

1 Introduction

The Pliocene Model Intercomparison Project Phase 2 (hereafter PlioMIP2; Haywood et al. (2016)) has dual focus: 1) to improve understanding of Pliocene climate and 2) to evaluate climate model uncertainty for a warmer than modern climate. This dual focus are referred to as Pliocene4Pliocene (P4P) and Pliocene4Future (P4F). PlioMIP2 concentrates on a 'time slice' centred on an interglacial peak (Marine Isotope Stage (MIS) KM5c; 3.205 Ma) within the mid Piacenzian, for convenience we refer to this as the *Pliocene*. The overall PlioMIP2 experiment design is split up into three components - CORE, Tier 1 and Tier 2 experiments. The CORE components must be completed by all modelling groups, whilst the Tier 1 and Tier 2 components are optional with Tier 1 experiments being a higher priority than Tier 2. The PlioMIP2 protocol specifies a standard and enhanced boundary condition dataset. The standard boundary conditions have a Pliocene topography constrained by the modern land sea mask (LSM) and bathymetry, whilst the enhanced boundary conditions have full PRISM4 mid Piacenzian palaeogeography (Pliocene Research Interpretation and Synoptic Mapping; Dowsett et al. (2016)). Here we describe the model set-up of the enhanced boundary conditions within HadCM3 (Hadley Centre Climate Model version 3). Table 1 details the PlioMIP2 experiments conducted within this study, along with an additional set of non-PlioMIP2 experiments that explore

specific model sensitivities. We conduct all CORE and Tier 1 experiments as well as the Pliocene4Future Tier 2 experiments as described within Haywood et al. (2016).

The structure of this paper is as follows. Section 2 describes the model configuration. Section 3 describes the experiment design including model boundary conditions, model initialisation and spin-up. Results from the experiments are then described within Section 4, with a particular focus on atmospheric circulation and surface climatology (Section 4.1) and the oceanic responses (Section 4.2).

2   Model Description

We use the UK Meteorological Office (UKMO) HadCM3 coupled Atmosphere-Ocean General Circulation Model (AOGCM). A top-level description of the atmosphere and ocean models relevant to this palaeogeographic reconfiguration follows. A focus is given to the ocean model as its external geometry is changed (the atmosphere model layers drapes over the topography) and certain aspects impact upon the interpretation of model prediction. For a more comprehensive description of the fundamental model structure see Pope et al. (2000) and Gordon et al. (2000). Subsequent corrections and improvements to the model, as well as a thorough evaluation against observational data has been described in Valdes et al. (2017). The HadCM3 model used in this study is equivalent, in terms of model updates and modifications, to HadCM3B-M2.1a of Valdes et al. (2017). We keep with the name HadCM3 in reference to the UKMO (Pope et al., 2000; Gordon et al., 2000) but acknowledge the contribution made by the University of Bristol in keeping the HadCM3 model developed and updated.

The HadCM3 climate model is no longer state-of-the-art but the model's runtime speed, relative ease of reconfiguration, and prediction performance make it well suited for a suite of centennial scale palaeoclimate simulations as is required here. HadCM3 can be integrated for many thousands of model years and reaches a satisfactory state of equilibrium with little drift in the surface climatology. However, there are a number of model weaknesses, compared to more contemporary models, and these will be discussed where relevant.

The HadCM3 model has been used extensively for studies of the Pliocene. The model was used within PlioMIP1 experiments 1 (Atmosphere GCM) and 2 (Atmosphere-Ocean GCM; Bragg et al. (2012)), and amongst others has been used to successfully investigate Panama Seaway closure (Lunt et al., 2008), ENSO and teleconnections (Bonham et al., 2009), ice sheet reconstructions and orbital forcing (Dolan et al., 2011; Prescott et al., 2014), sea ice reconstructions (Howell et al., 2014), terrestrial and marine oxygen isotopes (Tindall and Haywood, 2015), and non-analogous aspects of Pliocene climate (Hill, 2015). In all cases, either a modern LSM and bathymetry was used or specific regional palaeogeographical uncertainties were explored. This body of work therefore represents the first published record where HadCM3 has been reconfigured with a bespoke global Pliocene palaeogeography.

2.1   Atmosphere model

The atmosphere component of HadCM3 has 19 vertical hybrid sigma-pressure levels extending to 5 hPa. Horizontal resolution is 3.75° longitude × 2.5° latitude. The model has a time-step of 30 minutes and is coupled to the ocean model (Section 2.2) at

2

the end of every model day (Gordon et al., 2000). Atmospheric composition, other than CO_2 (described in Section 3.1 and 3.2) is equivalent to pre-industrial throughout (N_2O 270 ppb, CH_4 760 ppb and no CFC) consistent with both the PMIP2 protocol (Braconnot et al., 2007) and the previous Pliocene experiments conducted within PlioMIP1. Monthly distribution of ozone is derived from the Li and Shine (1995) climatology and ground-based troposphere measurements, corrected for the ozone hole (Johns et al., 2003). The radiative effects of background aerosol are represented by a simple parameterisation based on modern climatological conditions (Cusack et al., 1998).

The solar constant (total solar irradiance; hereafter TSI) is held fixed at 1365 Wm^{-2} within all PlioMIP2 protocol experiments, a value consistent with the pre-industrial experiment within PMIP2 (the 2nd Palaeoclimate Model Intercomparison Project; LSCE (2007)) and CMIP5 (the 5th Coupled model Intercomparison Project; Taylor et al. (2012)) as well as PlioMIP1. This value (derived in the 1990s) is used to remain consistent with previous work but acknowledge that space borne measurements of TSI have decreased from 1371 to 1362 Wm^{-2} from 1978 to 2013 (Kopp and Lean, 2011; Meftah et al., 2014). Indeed, the CMIP6 pre-industrial simulation (piControl) uses a value of 1361 Wm^{-2} (Matthes et al., 2017). We examine the impact of TSI choice within the context of both pre-industrial and Pliocene climates within Section 4.3.2. Recognising this source of uncertainty and the impact on climate anomalies (due to non-linear climate responses) is important as the PlioMIP2 specification (Haywood et al., 2016, Section 2.3.1) leaves the choice of TSI to individual modelling groups, whose TSI may depend upon if the group is a participant of CMIP6. The impact of TSI choice is minimised by the Pliocene communities use of climatological anomalies, but should be considered when comparing model-model absolute indices (summer sea ice extent, AMOC strength, etc.).

The land surface scheme is MOSES 2.1 (Met Office Surface Exchange Scheme; Cox et al. (1999); Essery et al. (2003)) which principally deals with the hydrology of the canopy to the subsurface and the surface energy balance (including subsurface thermodynamics). Within the scheme there are 5 plant functional types (PFTs: broadleaf and needleleaf trees, C_3 and C_4 grasses, and shrub) as well as soil (desert), lakes and ice. Each non-glaciated terrestrial grid cell can take fractional values of each surface type.

The HadCM3 PlioMIP1 study of Bragg et al. (2012) used an earlier version of MOSES (MOSES1) which treats each model grid cell as a homogeneous surface and uses effective parameters to calculate the grid cell's energy and moisture flux. However, MOSES2 introduced subgrid (tiled) heterogeneity and improved representation of surface and plant processes such that hydrological partitioning and energy balance is computed for each subgrid tile. A comparison of MOSES1 and MOSES2.1 can be found within Valdes et al. (2017). In this study we incorporate a software update taken from the HadGEM2 climate model (Good et al., 2013) which corrects the temperature control of plant respiration and improves forest resilience to elevated temperatures (making the model MOSES2.1a in the nomenclature of Valdes et al. (2017)).

Runoff is collected in drainage basins and delivered to associated coastal outflow points (on a 3.75°×2.5° geographic grid). River transport is not modelled explicitly, instead runoff is returned to the coastal outflow point in the uppermost layer of ocean instantaneously at the atmosphere-ocean coupling step (Gordon et al., 2000). Internally-draining basins are present but the associated water loss is not explicitly modelled within the routing scheme. Instead, the loss of freshwater in the hydrological cycle is corrected using an artificial freshwater correction field applied to the uppermost surface of the ocean (Section 2.2). This freshwater closure also acts to correct the freshwater loss due to terrestrial snowfall accumulation.

2.2 Ocean Model

The ocean component is a rigid lid model of the Bryan-Cox lineage (Bryan, 1969; Cox, 1984). In the vertical there are 20 unevenly-spaced levels, concentrated near the surface in order to improve representation of the surface mixed layer. The model uses z co-ordinate vertical layers with bottom topography represented by "full" cells. This leads to a discontinuous representation of the bathymetry which has poorer fidelity at greater depths (where the thickness of levels is greatest). The ocean time-step is 1 hour and horizontal spatial resolution is $1.25° \times 1.25°$ and the grid is aligned so that there are six ocean grid cells to each atmosphere grid cell ($3.75° \times 2.5°$). To simplify coupling with the atmosphere model, the ocean model's coastline has a resolution of $3.75° \times 2.5°$ at the uppermost level.

Within the modern boundary conditions, cells overlying important subgrid-scale channels, such as those along the Denmark Strait, the Iceland-Faroe and the Faroe-Shetland Channels, and straits surrounding the Indonesian archipelago, are artificially deepened. Additionally, within the Greenland-Iceland-Scotland region, a convective adjustment scheme (Roether et al., 1994) is used to better represent down-slope mixing that improves the representation of dense outflows that form the North Atlantic Deep Water (NADW). The scheme is not used for Antarctic Bottom Water. Water mass exchange through the Strait of Gibraltar, a channel that falls subgrid-scale, is achieved with a diffusive pipe. This pipe provides transport of water properties through the 13 topmost layers of the ocean (~ 1200m) between the Eastern Atlantic with the Western Mediterranean. Other subgrid-scale channels, such as the Canadian Archipelago, Hudson Strait outflow and the Makassar Strait, remain spatially unresolved and therefore unrepresented. The latter has been shown to possess most of the Indonesian throughflow (Gordon and Fine, 1996) and so is compensated for within the model by a deepening of regional model bathymetry.

The fresh water budget of the ocean is balanced by fluxes from the river routing scheme and a freshwater correction applied to the uppermost ocean level. Within the pre-industrial (and associated CO_2 sensitivity experiments) the freshwater correction field is prescribed (time-invariant). The correction field had been derived to provided closure of the model's modern hydrological cycle and consists of a uniform background component (0.01 mm day^{-1}) correcting internal-drainage (Section 2.1) and an iceberg component (0.02 mm day^{-1}) whose geographic distribution is derived from modern observations (Gordon et al., 2000; Pardaens et al., 2003). Within the Pliocene experiments we omit the time-invariant correction (including the iceberg component) and instead use an annual model-derived geographically-invariant freshwater correction to reduce residual salinity drifts to zero. We justify this as we currently do not have *a priori* knowledge of the geographic distribution of iceberg melt consistent with the ice sheet distribution within the PlioMIP2 enhanced boundary conditions. In the Northern Hemisphere we do not expect significant iceberg calving given the configuration of the Greenland Ice Sheet and the lack of marine terminating margins specified within the PRISM4 boundary conditions.

The rigid lid streamfunction scheme imposes the need for bathymetry to be smoothed particularly in steep regions of the high latitudes, and for islands to be specified as line integrals for the barotropic stream function. A major consequence of the latter is that the modern Bering Strait throughflow is not fully resolved as it sits between two model-defined continents between which the barotropic component of flow is poorly resolved. This impacts our interpretation of the Pliocene experiments (closed

Bering Strait) with respect to the pre-industrial (open Bering Strait), this is discussed within Section 3.2.2. An advantage of the rigid lid scheme on the other hand is that barotropic gravity waves are neglected, which facilitates the use of longer time-steps.

The sea ice model is a simple thermodynamic scheme based upon Semtner (1976) with parameterisations for ice drift and concentration. To account for sea ice leads, upper-boundaries of 0.995 and 0.980 are imposed to Arctic and Antarctic sea ice concentrations based upon the parameterisation of Hibler (1979). Ocean salinity is influenced by sea ice formation and melt by assuming a sea ice salinity of 0.6 psu (excess salt, in effect, is returned to the ocean). Sublimation is represented and acts to increase ocean salinity (salt blown into leads), whilst ocean-bound snowfall and precipitation reduce salinity. The effects of snow age and melt pond formation on surface albedo are represented with a linear parametrisation based upon surface temperature. Ice drifts only by the action of surface ocean current, hence within the model surface wind stress indirectly influences sea ice drift via its influence on the surface ocean current. Sea ice dynamics is represented by parameterisations based upon Bryan et al. (1975). Ice rheology is simply represented by preventing ice convergence above 4 m thickness. There is no representation for the interaction between floes.

3 Experiment Design

Here we describe the setup of the Pliocene and the pre-industrial experiments. The Pliocene experiments have CO_2 set to 280, 350, 400, and 450 ppm, each conducted with modern orbit as specified by the PlioMIP2 protocol (Haywood et al., 2016). These experiments are labelled the *control* Pliocene experiment Eoi^{400} (PlioMIP2 CORE), $Eoi^{350,450}$ (Tier 1; P4F+P4P), and Eoi^{280} (Tier 2; P4F). Here we use a comma separated list in the superscript to indicate 2 or more experiments. In all cases, the superscript indicates CO_2 (in ppm) and the o and i indicate the inclusion of of the PRISM4 orography (including PRISM4 vegetation, soil, and lakes) and ice sheets. The experiments based upon the pre-industrial geography are run with CO_2 values of 280, 400, and 560 ppm. These are identified as the *control* pre-industrial experiment E^{280} (CORE), E^{400} (Tier 2; P4F) and E^{560} (Tier 1; P4F).

We explore two sets of non-protocol sensitivities - Pliocene orbital configuration and TSI. The PlioMIP2 protocol (Haywood et al., 2016) specifies a modern orbital configuration for all Pliocene experiments. We investigate the validity of this orbit choice by rerunning Eoi^{400} with a 3.205 Ma orbital configuration representing the mPWP time slice of Haywood et al. (2013a) within experiment $_{orb}Eoi^{400}$. We also investigate the choice of total solar irradiance (Section 2.1) by rerunning the two control (CORE) experiments with a TSI of 1361 Wm^{-2} within $_{1361}E^{280}$ and $_{1361}Eoi^{400}$.

In total 6 Pliocene experiments were run: the CORE (Eoi^{400}), two Tier 1 (Eoi^{350} and Eoi^{450}), one Tier 2 (Eoi^{280}) as well as an orbital ($_{orb}Eoi^{400}$) and TSI sensitivity experiment ($_{1361}Eoi^{400}$). These are accompanied by 4 pre-industrial based experiments: the CORE (E^{280}), a Tier 1 (E^{560}) and Tier 2 (E^{400}) as well as a TSI sensitivity experiment ($_{1361}E^{280}$). These 10 simulations are detailed within Table 1.

3.1 Pre-industrial and associated sensitivity experiments ($E^{280,400,560}$ and $_{1361}E^{280}$)

The experiments with pre-industrial geography are 500 year continuations of a long integration ($>$2000 model years) pre-industrial experiment that had been initialised from the observed ocean state of Levitus and Boyer (1994). The experiment uses a topography and a bathymetry regridded and smoothed from ETOPO5 (Edwards, 1989), and vegetation and soil translated from the land cover of Wilson and Henderson-Sellers (1985). River routing is derived by aggregating runoff in all terrestrial grid boxes within each runoff basin in a manner which is internally consistent with the model topography. All model boundary conditions were developed by the Met Office Hadley Centre (hereafter MOHC) and used within CMIP3/5. In accordance with the PlioMIP2 protocol (Haywood et al., 2016), levels of atmospheric CO_2 are set to 280, 400 and 560 ppm giving the pre-industrial (E^{280}) and two CO_2 sensitivity experiments (E^{400} and E^{560}). A fourth pre-industrial based experiment, $_{1361}E^{280}$, is run to investigate the model sensitivity to the choice in TSI value (Section 2.1 and 4.3.2).

3.2 Pliocene (PlioMIP2 enhanced) and sensitivity experiments ($Eoi^{280-450}$, $_{orb}Eoi^{280-450}$, and $_{1361}Eoi^{400}$)

3.2.1 Boundary condition preparation

For PlioMIP2 the boundary conditions for the modern day and the 'enhanced' variant of the Pliocene reconstruction are provided on regular 1° grids held within NetCDF files (USGS, 2016; Haywood et al., 2016). For convenience we shall refer to the PlioMIP2 enhanced boundary condition as PRISM4. The modern boundary condition is provided to facilitate the anomaly method of boundary condition generation. The LSM is first regridded by computing the anomaly of PRISM4 Pliocene minus modern (at 1° resolution) and regridding using bilinear interpolating to the 3.75°×2.5° model grid, and then applying the anomaly to the models pre-industrial LSM. This is so that the final reconstruction is consistent with both the original pre-industrial model set up and the PRISM4 LSM. Finally, a number of manual corrections were applied to the resulting 3.75°×2.5° PRISM4 LSM to ensure that the underlying character of the PRISM4 reconstruction is represented as best as reasonably practicable at the model's resolution. For consistency with the pre-industrial boundary conditions developed by MOHC we remove Svalbard and Novaya Zemlya, despite their subaerial extension within PRISM4. Similarly, we keep the Pliocene LSM in the Persian Gulf region the same as pre-industrial despite a withdrawal of the Persian Gulf within PRISM4. This choice was made as the Persian Gulf within the pre-industrial LSM is represented by an inland sea (due to inadequate spatial resolution) and so further changes would be difficult to interpret. At model resolution the Pliocene Strait of Gibraltar is identical to the pre-industrial and so the diffusive pipe is incorporated.

The resulting PRISM4 LSM was used to constrain the generation of the Pliocene orography and bathymetry (which was generated using area-weighted regridding, and then applied as an anomaly to the existing HadCM3 pre-industrial orography and bathymetry). River basins and outflow points were derived from the pre-industrial routing scheme (Section 3.1) but corrected in regions of LSM, topographical and ice-bedrock change using a model-resolution river routing model based on the D8 method (Tribe, 1992). This was then followed by manual correction in regions when model resolution fails to capture important orography, or where the regridded Pliocene orography is flat. The PRISM4 vegetation scheme (represented by BIOME4 biomes) was regridded by combining a BIOME4-to-MOSES2 lookup table with an area-weighted survey of underlying biomes. A similar

area-weighted regridding was conducted for the lake field. We chose not to generate the lake field as an anomaly from the modern lake distribution as land surface change since the pre-industrial would be imprinted on the model's lake distribution.

3.2.2 Barotropic streamfunction island configuration

Rigid lid Bryan-Cox type models, such as the ocean of HadCM3, require islands (and by extension, continents) to be identified so that a net non-zero barotropic flow (depth-independent) can be achieved around the line integral (streamfunction non-zero). The default pre-industrial configuration of the model has 6 islands defined and is shown within Figure 1. For consistency, aforementioned (Section 3.2.1) manual corrections to both LSM and bathymetry have allowed islands to be specified that are consistent with the E^{280} experiment, but also reflect the key palaeogeographic changes presented by the PRISM4 palaeogeography. In particular western Iceland and East Greenland land cells were adjusted to ensure that Iceland could be defined as a streamfunction island (Figure 1), and hence we could fully represent the East Greenland Current. The island to the west of the Antarctic Peninsula body lies within the island definition of the main Antarctic continent and therefore the circulation between the two is not fully resolved (only the baroclinic flow is resolved fully). Figure 1 compares the pre-industrial and PRISM4 Pliocene HadCM3 island specification, It can be seen that the 6 islands in the pre-industrial configuration has been increased to 8 islands in the Pliocene.

It is noted that within the pre-industrial HadCM3 model setup the Bering Strait barotropic component of throughflow is unresolved and both the Makassar Strait and the Canadian Archipelago are spatially unresolved (Section 2.2). This poses a conceptual problem in the interpretation of the Pliocene experiments with respect to the pre-industrial, as the PRISM4 Pliocene geography has these throughflow regions closed. Therefore, our simulations do not resolve the full climatic response of these regional palaeogeographic changes. A pre-industrial experiment with a fully-resolved Bering Strait and Canadian Archipelago would partially address these problems but would then force a divergence away from the previous HadCM3 descriptions and evaluations, as well as from past and current CMIP/PMIP and PlioMIP1 model implementations. These problems are likely to arise in all rigid lid streamfunction ocean models that have insufficient spatial resolution to fully-resolve these gateways and inherently cannot resolve line integrals around bounding land masses. Ocean models that have explicit or implicit free surface schemes with sufficiently high horizontal spatial resolution may reduce these issues.

3.3 Pliocene Model initialization and spin-up

Model spin-up is conducted in a series of stages in which the model and boundary conditions are increased in complexity. These stages are:

1. The atmosphere model (AGCM) was initialized in a 50 year run with PRISM4 LSM and basic surface scheme (lakes, ice, shrubs and orography), pre-industrial CO_2 (280 ppm) and zonal hemispheric-symmetric monthly Sea Surface Temperature (SST) and sea ice distribution derived from the initial 2500 model year pre-industrial HadCM3 simulation from Section 3.1. Model failures at this stage allow for the identification of steep topography that requires regional smoothing.

2. The ocean model is added (without barotropic physics) and the resulting AOGCM run is continued for 100 years with Pliocene bathymetry and river scheme (year 50 within Figure 2).

3. Barotropic physics is incorporated (without specifying islands) and the simulation is continued run for 200 years. Regional bathymetric smoothing was applied in regions which caused model failure (Figure 2 stage a).

4. The island configuration (Section 3.2.2, Figure 1) is then derived using an iterative series of sensitivity tests in which each island configuration is refined. Once complete, the set of island line integrals are incorporated into the model configuration. At this stage we have an AOGCM incorporating full barotropic physics (Figure 2 stage b).

5. CO_2 is increased from 280 ppm at 1% per year until 400 ppm is attained. CO_2 is then held fixed.

6. At model year 950 a problem with ancilliary file generation had been resolved allowing the vegetation boundary condition to be incorporated into the model. Additionally, a regional modification was made to the bathymetry and streamfunction island configuration to the west of the Antarctic Peninsula to resolve a persistent numerical mode within the barotrotopic solver in this region (Figure 2 stage c).

7. The AOGCM model was then set to continue to year 2000 (CO_2 held fixed at 400 ppm).

8. At year 2000, five additional experiments are spun-off that run alongside Eoi^{400} (Table 1), these are $Eoi^{280,350,450}$, $(_{orb}Eoi^{400})$ and $_{1361}Eoi^{400}$. All six experiments are run to year 2400.

9. The models are then run for the final 100 years configured with full climatological output.

3.4 Equilibrium State

By model years 2400 to 2500, the Pliocene control experiment (Eoi^{400}) has achieved a quasi-steady-state equilibrium in which the globally-integrated net top-of-the-atmosphere (TOA) radiative imbalance is 0.047 Wm^{-2}, surface 1.5 m air temperature trend is 0.08°C century^{-1} and ocean potential temperature trends within the upper 200 m and globally integrated are -0.026°C century^{-1} and 0.041°C century^{-1}. The corresponding values for the pre-industrial control experiment (E^{280}) are -0.115 Wm^{-2}, 0.052°C century^{-1}, 0.008°C century^{-1} and -0.014°C century^{-1} respectively. High CO_2 experiments, Eoi^{450} and E^{560} present the largest, yet modest departures from equilibrium and are characterized by TOA imbalance >0.2 Wm^{-2}. Positive TOA imbalance is indicative of a warming of the earth system, the small heat capacity of the atmosphere means that residual energy is predominantly taken up by the ocean, which is reflected in the volume integrated ocean temperature evolution. Warming of the deep ocean is primarily occurring at depths deeper than 2000 m in the Pacific basin. The Indian and Antarctic oceans are the most equilibriated, particularly at intermediate depths and deeper. Table 2 summarizes the equilibrium states of the seven PlioMIP2 experiments and Figure 2 presents the time-evolution of ocean potential temperature of the Pliocene control experiment (Eoi^{400}). All experiments are deemed to be in a satisfactory state of equilibrium, although the high TOA simulations Eoi^{450} and E^{560} have above average warming within the deep ocean.

4 Results

We base our analysis on climatological averages from the final 50 years of each simulation. The final 50 years of output is used to remain consistent with the HadCM3 PlioMIP1 submission (Exp. 2 of Bragg et al. (2012)). The PlioMIP2 protocol (Haywood et al., 2016) does not state a standardised time length for climatological means although the PlioMIP2 website (USGS, 2018) does request 100 years of monthly climatology. We therefore make the 50 year climatological average and 100 years of monthly climatology available on the PlioMIP2 data repository.

In order to keep discussion clear and concise, we principally compare the two PlioMIP2 CORE experiments which we refer to as the *control* experiments (Eoi[400] and E[280]). Whilst there is uncertainty in mid Piacenzian (MIS KM5c) CO_2 levels, 400 ppm represents the middle of the anticipated CO_2 range derived from marine and terrestrial based reconstructions. We therefore consider Eoi[400] as our "best estimate" simulation. In addition, when referring to climate forcing, we use the term *palaeogeography* to encompass the combined change in topography, land surface (vegetation, lakes, soils, ice sheets), LSM and bathymetry which we diagnose from the anomaly Eoi[280] minus E[280].

4.1 State of the atmosphere and earth surface climatology

4.1.1 Surface Air Temperature and Climate Sensitivity

Modelled mean annual 1.5 m surface air temperatures (hereafter MASAT) are detailed within Tables 3 and corresponding Pliocene anomalies are shown within Figure 3. Relative to the pre-industrial control (E[280]) temperatures are generally warmer within the Pliocene experiments. Differences in MASAT of up to 31.3°C over Greenland and Antarctic regions coincide with Pliocene ice sheets and where their respective elevation is less than the pre-industrial. Typically, warming is greatest over land, although in ocean regions at or near Antarctic LSM change (pre-industrial grounded ice to Pliocene ocean) warming is significant. This pattern of warming is similar to results derived with HadCM3 within PlioMIP1 under PRISM3 boundary conditions (Exp. 2 of Bragg et al. (2012)).

The Pliocene cooling in the Barents Sea is statistically significant and persistent through the model integration (Figure 3). It coincides with an increase in Pliocene winter and spring sea ice concentration driven by palaeogeographic terrestrial winter cooling in the circum-Arctic (Pliocene subaerial Barents and Baltic Sea). This cooling is potentially driven by the partial suppression of northward heat transport (in the Norwegian Current) by the subaerial extension of Ireland and Scotland within the model.

The Eoi[400]-E[280] MASAT anomaly of 2.9°C (Table 3) is lower than the 3.3°C of HadCM3 within PlioMIP1 (Bragg et al., 2012) and lies within the PlioMIP1 model ensemble range of 1.84 - 3.60°C (Haywood et al., 2013b). The MASAT anomaly also lies between the PlioMIP2 studies of 2.4°C Kamae et al. (2016) and 3.8°C (Chandan and Peltier, 2017), although note that this comparison is not exhaustive as PlioMIP2 is incomplete at the time of press. Table 3 also presents MASAT data for the equatorial (between 30°S and 30°N) and polar regions (latitudes greater than 60°). The resulting polar amplification factors for the Pliocene control (Eoi[400]) relative to the pre-industrial control (E[280]) are 1.7 for the North Pole and 2.2 for the South Pole.

30   Figure 4 shows the annual and seasonal temperature anomalies for Eoi^{280} and Eoi^{400} (against E^{280}). Terrestrial regions that are subaerial only within the Pliocene, such as the Hudson Bay and the Baltic Sea regions are up to 10°C warmer (colder) during the summer (winter) seasons, due to land-ocean heat capacity contrast. It is unclear how much of this seasonal temperature response in the Baltic Sea region (subaerial during the Pliocene) is a driver of persistent cooling within the Barents Sea region.

From the results in Table 3 it is possible to diagnose the factors that contribute to Pliocene warming relative to the pre-industrial (E^{280}). Considering the Pliocene control experiment (Eoi^{400}), we find that the change in palaeogeography (Eoi^{280}-E^{280}) accounts for a temperature change of 1.4°C, whilst the increase in CO_2 (Eoi^{400}-Eoi^{280}) accounts for a further 1.5°C of

5   warming. Considering uncertainty in Pliocene CO_2 level, we find temperature changes of 0.9 and 2.0°C for Eoi^{350}-Eoi^{280} and Eoi^{450}-Eoi^{280} respectively. The PlioMIP2 experimental design provides a second pathway to examine Pliocene palaeogeographical and CO_2 forcing (e.g. Eoi^{400}-E^{400} and E^{400}-E^{280}). Within this pathway, the Pliocene geography (Eoi^{400}-E^{400}) accounts for 1.8°C of warming and the increase in CO_2 (E^{400}-E^{280}) accounts for 1.1°C of temperature increase. These differences highlight that there are non-linearities within the climate system's response to changes in boundary condition.

10   The climate system's sensitivity to a doubling of CO_2 (Climate Sensitivity; CS) is 3.5°C for the pre-industrial (derived from E^{560} and E^{280}) and 2.9°C for the Pliocene (derived from Eoi^{400} and Eoi^{280} and scaled by 1.94 (=log(560/280) / log(400/280)). The pre-industrial CS is consistent with the 3.3°C for HadCM3 within CMIP3 (Randall et al., 2007). The Pliocene CS is similar to the 3.1°C for HadCM3 and lies at the lower end of the 2.7 - 4.1°C ensemble range of PlioMIP1 Experiment 2 (Haywood et al., 2013a). When we approximate Earth System Sensitivity (ESS) using Eoi^{400} and E^{280} (with ESS = 1.94 x $\triangle T_{Eoi^{400} - E^{280}}$)

15   we obtain ∼5.6°C. Subsequently the ESS/CS ratio is ∼1.9, which lies at the higher-end of the 1.1 - 2.0 range of the PlioMIP1 ensemble (Haywood et al., 2013a) in which HadCM3 had a ratio of 2.0. It must be noted, however, that this calculation assumes that the PlioMIP2 enhanced boundary condition *represents* the equilibriated Earth System under a contemporary doubling of CO_2, hence neglecting non-glacial elements of the PRISM4 retrodicted palaeogeography.

4.1.2 Precipitation

20   The globally integrated Mean Annual Precipitation (MAP; Table 4) is influenced by both Pliocene geography and CO_2 changes. Pliocene geography acts to increase globally integrated MAP, although this appears sensitive to the background CO_2 level (e.g. Pliocene geography increases MAP by 0.07 and 0.05 mm day^{-1} at 280 and 400 ppm respectively). The Eoi^{400}-E^{280} MAP anomaly of 0.11 mm day^{-1} (Table 4) compares with the 0.17 mm day^{-1} from HadCM3 within PlioMIP1 (Bragg et al., 2012) and sits at the lower end of the ∼ 0.09 - 0.18 mm day^{-1} of the PlioMIP1 model ensemble (Haywood et al., 2013b).

25   The geographical distribution of MAP change can be seen within Figure 5. Northern Hemisphere land masses generally see increased precipitation within the Pliocene although this effect is minimal in the continental interiors. In the Southern Hemisphere much of South America and South Africa receives less precipitation whilst Australia and Northern Greenland see an increase in precipitation during the Pliocene. Increasing Pliocene CO_2 generally intensifies the precipitation anomaly which is most apparent in the tropics. Regions that receive little precipitation within E^{280} e.g. North Africa and the East Antarctic Ice

30   Sheet have little (<0.1 mm day^{-1}) change in precipitation under increasing Pliocene CO_2.

Seasonal plots of precipitation change between the Pliocene (Eoi^{400}) and the pre-industrial (E^{280}) control experiments are shown in Figure 6. During the Pliocene we see wetter summers over much of North America and northern Europe. Regions experiencing reduced precipitation in western North America as well as central and western Europe are a consequence of weakened westerlies (not shown). As can be seen within Figures 6(c-f), the Pliocene geography and land surface change drive an intensification of precipitation associated with the Inter Tropical Convergence Zone (ITCZ), although changes in seasonal latitudinal distribution are not evident. The South Pacific Convergence Zone, extending from the Western Pacific warm pool (WPWP) southeastward to the South Central Pacific extends ~15° further east in E^{280} than Eoi^{400} and Eoi^{280}.

4.1.3 Planetary scale atmospheric circulation.

The time averaged, zonal mean, meridional mass stream function for the atmosphere is shown within Figure 7. Clearly distinguished are the Hadley, the Ferrel and the Polar cells. The mean meridional circulation is sensitive to equatorial asymmetries in surface temperatures as ascent in the tropical belt and subsidence in the subtropics form the Hadley cells. Taking the maximum of the meridional streamfunction as a measure of the Hadley cell strength, we find that the Pliocene geography acts to weaken (intensify) the Hadley cell within the Northern (Southern) Hemisphere. Looking at E^{280} we find the northern cell is stronger (+10.8%) than the southern cell which is in contradiction with observational and re-analysis data (Stachnik and Schumacher, 2011) that consistently shows the southern cell being stronger than the northern cell. With increasing Pliocene CO_2, the southern cell intensifies and becomes stronger than the north (+19% in Eoi^{280} and +42% in Eoi^{400}). This intensification (weakening) of the Hadley cell under changed land surface and geography should be driven by steepening (shallowing) of the tropical meridional temperature gradients in the Tropics south (north) of the ITCZ. Coincident with the change in land surface and geography (Eoi^{280}-E^{280}) is a weakening of the combined annual mean overturning within the two Hadley cells (191 and 180 x10^9 Kg s^{-1} for E^{280} and Eoi^{280} respectively).

The wintertime Subtropical Jet (StJ; also known as the midlatitude jet) and Polar Jet (PJ) are shown within Figure 8. We characterise the mean spatial envelope of the jet path by deriving from 50 years of daily data, the days per season in which the mean mass-weighted flow speed integrated over 400-100 hPa (~7-16 km) exceeds 30 ms^{-1}. For both E^{280} and E^{400} we obtain a seasonal jet stream configuration which is consistent with the ERA-40 and derived results of Archer and Caldeira (2008). The PJ and the StJ stream can be difficult to differentiate as the former is latitudinally irregular, so following Koch et al. (2006) we use normalised wind shear as a height differentiator. The StJ stream path is more persistent and stable and so is characterised by the mean latitude of the StJ core which is shown within Table 5. The change in geography (Eoi^{280}-E^{280}) drives a poleward shift of the mean StJ latitude of ~1.6° in the Northern Hemisphere (both seasons) and 2.2° in the Southern Hemisphere summer. The response to Pliocene CO_2 (Eoi^{400}-Eoi^{280}) increase is weaker with a 0.8° poleward shift of the mean StJ latitude in the Northern Hemisphere (both seasons). The Southern Hemisphere mean StJ appears only weakly poleward shifting in response to Pliocene CO_2 increase. Regionally, jet behaviour deviates from the global mean view. Within the North Atlantic, the PJ moves equatorward in response to the change in palaeogeography (Eoi^{280}-E^{280}) moving the jet stream mean path from northern to southern Europe (Figure 8b vs. 8f). Synoptic storms grow and propagate along jet stream axis and so

this equatorward shift in the PJ likely contributes to the increase in rainfall seen in southern Europe during Pliocene wintertime (Figure 6e vs. 6f).

4.2 State of the Ocean climatology

4.2.1 Sea surface temperature and warm pools

Modelled mean annual SST's (MASST) are detailed within Table 6 and Pliocene anomalies are shown within Figure 9. We see a 0.8°C warming due to the change in palaeogeography (Eoi^{280} -E^{280}) and a further 1.0°C of warming due to the change in Pliocene CO_2 (Eoi^{400} -Eoi^{280}). With increasing levels of CO_2 regional patterns of MASST change due to palaeogeography are overprinted by CO_2-induced warming. This warming is most evident in the mid-latitudes, particularly within the North and South Atlantic and the North Pacific. The greatest warming occurs within the North Atlantic subpolar gyre where Eoi^{400} -E^{280} reaches 9.3°C. In the vicinity of the modern Gulf Stream and North Atlantic Drift we find a cooling during DJF and MAM seasons (up to -4.9°C within Eoi^{280} -E^{280}). Investigation of surface ocean vectors (not shown) suggests an intensification of the North Atlantic wind-driven subpolar gyre and Labrador current which appears to disrupt western intensification and the path of the Gulf Stream. The westerlies in the region appear to intercept the remnant gulf stream and divert it from a north easterly to a more eastward path, this is seen as the warm tongue south of the extant Gulf stream (Figure 9). A similar expression of MASST within the North Atlantic was seen by Chandler et al. (2013) and characteristic signatures may be present within other PlioMIP1 experiments (e.g. Figure 1 of Dowsett et al. (2013)). A persistent cooling is also found within the Barents Sea region coincident with the surface air temperature anomalies discussed within Section 4.1.1.

Table 6 also details the size of the global and component equatorial warm pools within the pre-industrial and Pliocene experiments. We see an expansion of the globally-integrated warm pool with the change in palaeogeography (Eoi^{280} -E^{280}), but this effect diminishes with increased CO_2. This is evident in both the Western Hemisphere warm pool (WHWP) and Indo-Pacific warm pool (IPWP) regions. As expected, increased CO_2 drives warm pool expansion.

4.2.2 Sea Ice

A complex picture emerges in the sensitivity of seasonal sea ice distribution to geographic and CO_2 changes as shown within Figure 10. Within the Northern Hemisphere winter, the palaeogeography changes drive an equatorward expansion of sea ice in the Greenland Sea region. Increasing CO_2 from 280 to 400 ppm counteracts some of this expansion. In the Southern Hemisphere the palaeogeographical changes suppress sea ice extent significantly within the Weddell Sea and also eastward towards the Davis Sea in both summer and winter. Coincident with this suppression is an equatorward expansion of sea ice within the Bellinghausen Sea region. As we increase CO_2 we see a general reduction in the sea ice extent and concentration in both summer and winter months. Within Eoi^{400} boreal summer the Arctic is largely ice-free, the ice that is present is mostly <50% concentration. During austral summer the concentration of sea ice within the Pliocene becomes more asymetric and reduced in extent, being concentrated in the highest latitudes off the coast of West Antarctic.

4.2.3 Mixed layer depth and deep water formation

The mixed layer depth (MLD) for E^{280}, Eoi^{280} and Eoi^{400} is shown within Figure 11. We focus on deep convection, the principle mechanism of deep-water formation. Deep convection is highly localised and therefore model representation is only suggestive. Nevertheless, E^{280} represents reasonably well the modern open-ocean deep convection that occurs within the Weddell and Ross Seas (which form the main formation sites of Antarctic Bottom Water) and in the Labrador, Irminger and Greenland Seas. All Pliocene experiments exhibit more widespread deep convection particularly within the Labrador and Norwegian Seas, and near the Antarctic Peninsula island. In contrast to Burls et al. (2017) we do not model any significant increase in Pliocene North Pacific MLD, and hence no subsequent intensification of North Pacific Deep Water (NPDW) formation (Table 7 and Figure 11).

4.2.4 Ocean Heat and Mass Transports (Atlantic and Pacific MOC)

The Atlantic Meridional Overturning Circulation (AMOC) streamfunctions for E^{280}, Eoi^{280} and Eoi^{400} are shown within Figure 12 and detailed within Table 7. The pre-industrial experiment E^{280} has a maximum AMOC strength at 26.5°N of 13.4 ± 1.2 Sv. This compares reasonably well with the estimate of 17.2 ± 4.6 Sv derived by McCarthy et al. (2015) using measurements from the RAPID array between April 2004 and October 2012. The all-latitude maximum in AMOC strength ($AMOC_{max}$) within E^{280} occurs at ∼650 m depth at 33.75°N with a strength of 15.7 ± 1.2 Sv.

We find an AMOC which is more intense in the Pliocene than in the pre-industrial, which is accountable to the Pliocene palaeogeography (Table 7). The $AMOC_{max}$ of Eoi^{400} is 19.6 ± 1.0 Sv and occurs at ∼650 m depth at 33.75°N. Multidecadal to centennial fluctuations, including a dominant ∼225 year oscillation, are present within the Pliocene experiments but not the pre-industrial experiment. In all Pliocene simulations, $AMOC_{max}$ occurs within the 25 - 33.75°N zonal envelope and at a depth of ∼650 m. The Eoi^{400} $AMOC_{max}$ lies within the 10-24.6 Sv range of PlioMIP1 (Zhang et al., 2013), whilst the Eoi^{400}-E^{280} $AMOC_{max}$ anomaly of 4.2 Sv (Table 7) lies outside the PlioMIP1 ensemble range of -0.9–3.6 Sv.

Despite an intensification of the AMOC within the Pliocene experiments, we find that the overturning strength reduces slightly at ∼40°N driven by the changed land surface and bathymetry (Eoi^{280}-E^{280}). This is seen within cooling evident in Gulf Stream MASSTs of Figure 9. Under increasing Pliocene CO_2, the mid-latitude overturning intensifies with a corresponding decrease in the Gulf Stream MASST cold anomaly. The overturning within the polar region is evidence of bottom water formation within the Nordic Seas. In E^{280} overturning extends to ∼80°N but is weaker than in the Pliocene models (which extends to ∼75°N). This is reflected within the geographic extent and intensity of deep convection shown within Figure 11.

The Pacific Meridional Overturning Circulation (PMOC) streamfunction is shown within Figure 13 and detailed within Table 7, in which $PMOC_{+ve}$ reflects the strength of the subtropical gyre circulation whilst $PMOC_{-ve}$ reflects the strength (and depth) of the Pacific Deep Water (PDW) and North Pacific Deep Water (NPDW). Pliocene palaeogeography (Eoi^{280}-E^{280}) drives an intensification of both the subtropical gyre and PDW overturning, whilst increasing CO_2 acts to weaken them. The Pliocene subtropical gyre ($PMOC_{+ve}$) and PDW ($PMOC_{-ve}$) overturning are stronger regardless of CO_2 level (e.g. within Eoi^{400} $PMOC_{+ve}$ and $PMOC_{-ve}$ are 22% and 6% stronger than E^{280}). With the change in palaeogeography (Eoi^{280}-E^{280}) the PDW

shoals (from $\sim$4 to 3 km) and with increasing Pliocene CO_2 the NPDW overturning reduces in northward reach, associated with the warming of North Pacific MASST (Figure 9).

4.2.5 Antarctic Circumpolar Current

The Antarctic Circumpolar Current (ACC) strength is detailed within Table 8 and shown within Figure 14. We calculate the volumetric flow of the ACC at the Drake Passage across a 64.4-56.9°S, 65°W transect using the positive aspect of the U component (zonal) of the total (barotropic and baroclinic) velocity. We find an overly intense ACC within E^{280} and E^{400} when compared against recent observations of 134-164 Sv (Cunningham et al., 2003; Griesel et al., 2012). The overly intense ACC within HadCM3 has been identified previously. Meijers et al. (2012) compared CMIP5 historical experiments to observations

5 and found the model's ACC flow at the Drake Passage transect of 244.5 $\pm$ 4.0 Sv compared unfavourably to observations and 155 $\pm$ 51 Sv of the CMIP5 multi-model mean. This unrealistic intensity appeared to be driven, or at least connected to, an overly strong salinity gradient across the ACC, particularly towards low-latitudes (Meijers et al., 2012). This could be a consequence of the artificial fresh water correction field used within the CMIP5 historical and piControl experiments and the E^{280} here.

10   Modelled ACC strength appears significantly reduced within the Pliocene experiments. Westerlies intensify in the Southern Hemisphere within the Pliocene but mostly in regions poleward of the Sub-Antarctic front (poleward of the ACC). The weakened Drake Passage throughflow is mirrored within the vertically integrated barotropic stream function. Care must be taken when interpreting ACC strength in situations of changed palaeogeography and island specification. The ACC is weakly stratified and vertically coherent and so is dominantly barotropic in nature. Within the Pliocene boundary conditions (Section

15 3.2.2) the island Peninsula is defined as a separate barotropic island (from the Antarctic continent), and this may be driving the Pliocene reduction in ACC strength. Also given a more complex line-integral configuration, the model's barotropic solver may not be converging fully towards a solution. The change in island specification may also be responsible for the change in ACC geographical extent shown within Table 8. Defining the streamfunction cross section by the latitudes of the centroid and upper 50% of zonal transport we see that the change in geography (from E^{280} to Eoi^{280}) drives a general latitudinal thinning of the

20 ACC extent and an equatorward shift of its centroid.

    Within the Pliocene experiments, the ACC runs mostly between the surface and sea floor between 60 and 57°S, whilst a deeper countercurrent is present closer to the Peninsula. In the Pacific, a pronounced thinning of the ACC latitude extent is observed in which the Sub Antarctic front moves equatorwards (the subtropical front is mostly unchanged). With the Pliocene geography, there are suggestions that the Antarctic Coastal Current (the counter-current to the ACC) flows between the Penin-

25 sula island and the Antarctic land mass. There is uncertainty as smaller islands in this region are unrepresented within the model. Figure 14 also suggests a more continuous coastal current with the Pliocene palaeogeography, particularly between 180 and 90°E. The Antarctic Coastal Current plays an important role in air-sea exchange in the Weddell Sea region, leading to deep convection. This enhanced deep convection within the Pliocene is reflected within Figure 11 and would explain the strengthened AMOC within the Pliocene (Section 4.2.4), although the limited representation of deep convection within the

30 model should be noted. This intensified Antarctic Coastal Current is driven partially by intensified winds poleward of the Sub-

14

Antarctic front (at latitudes $>66°$S) within the Pliocene. The Weddell Sea sub-polar gyre is weakened and restructured whilst the Ross Sea gyre is less intense and extends more equatorward.

4.3 Sensitivity to external boundary conditions

4.3.1 Orbital configuration

Here we examine the sensitivity of the Pliocene climate to choice of orbital configuration (e.g. modern (default) vs. KM5C at 3.205 Ma). For Eoi^{400} there is no meaningful difference in global means (Table 3 MASAT, Table 4 MAP, Table 6 MASST and warm pool areal extent).

5   There is a statistical significant difference between $_{orb}$Eoi^{400} and Eoi^{400} AMOC$_{max}$ (t(98)=7.20, p<<0.0001) and AMOC$_{max}$ 26.5°N (t(98)=11.36, p<<0.0001) using a 2-sample t-test assuming unequal variance (null hypothesis being there is no difference in the two timeseries of annual means). With regards to PMOC$_{+ve}$, $_{orb}$Eoi^{400} and Eoi^{400} are deemed equivalent (t(98)=0.62, p=0.54) whilst for PMOC$_{-ve}$, the two experiments are equivalent at the 95% confidence level (t(98)= 1.93, p=0.06). Centennial-scale fluctuations in Pliocene AMOC$_{max}$ could account for statistical differences between the climatological mean periods of 10 $_{orb}$Eoi^{400} and Eoi^{400}, as AMOC$_{max}$ differences could simply reflect a lack of coherence introduced since the year 2000 fork point.

4.3.2 Total Solar Insolation

Section 2.1 identified the possibility of different TSI values being used within PlioMIP2 climate models. Here we determine the sensitivity of HadCM3 within E^{280} and Eoi^{400} experiments to changing the TSI parameter. Reducing total solar insolation 15 from 1365 to 1361 Wm^{-2} (- 0.3%) reduces the mean incoming solar (SW) radiation averaged over the entire Earth's surface by 1 Wm^{-2} (from 341.25 to 340.25 Wm^{-2}). Table 9 accumulates climatological indices from E^{280} and Eoi^{400} under these two TSI values. Figure 15 shows the spatial pattern of climatological differences (Pliocene minus pre-industrial) for simulations based upon 1365 and 1361 Wm^{-2} for MASAT, MAP and MASST. Overall the patterns of climatological anomalies for the experiments using TSI of either 1361 or 1365 Wm^{-2} are very similar. In this sense, comparison of model temperature anomalies to proxy 20 temperature anomalies should not generally be influenced by the choice of TSI.

    However, in a similar way to the orbital configuration, AMOC$_{max}$ does appear sensitive to TSI value when we compare Eoi^{400} against $_{1361}$Eoi^{400} (t(98)=-13.3, p<<.0001) and E^{280} to $_{1361}$E^{280} (t(98)=2.47, p=0.015). It is possible that this sensitivity to TSI could be a consequence of the previously described AMOC cyclicity and lack of coherence between Eoi^{400} and $_{1361}$Eoi^{400}.

5 Discussion

25 In this study we have described the incorporation of PlioMIP2 (PRISM4) mid-Piacenzian (Pliocene) enhanced boundary conditions into the HadCM3 global climate model. We conducted PlioMIP2 CORE and Tier 1 pre-industrial and Pliocene based

experiments as well as sensitivity experiments exploring solar insolation and orbit choice. We then examined the large-scale features of the atmosphere and ocean state of these experiments.

Comparing to the pre-industrial control (E^{280}), we find Pliocene surface warming focussed within the high-latitudes in a similar distribution to HadCM3 within PlioMIP1 under PRISM3 boundary conditions (Bragg et al., 2012). We find that the Pliocene palaeogeography and 400 ppm CO_2 account for a warming (relative to the pre-industrial) in globally integrated MASAT (and MASST) of 1.4°C (0.8°C) and 1.5°C (1.0°C) respectively. We derive climate sensitivities of 3.5°C and 2.9°C for the pre-industrial and Pliocene, which again are similar to results of PlioMIP1 of 3.3°C and 3.1°C respectively (Haywood et al., 2013a). We derive an approximation of Earth System Sensitivity of ~5.6°C leading to an ESS/CS ratio of ~1.9, which is similar to the ESS/CS ratio of 2.0 derived within PlioMIP1 (Haywood et al., 2013a). This similarity between PlioMIP1 and PlioMIP2 CS and ESS/CS ratio demonstrates an insensitivity of these quantities to the degree of palaeogeographic variation between PlioMIP1 and PlioMIP2. This strongly indicates that the primary control on the ESS/CS ratio is the reconstructed ice distribution and global vegetation coverage which, with the exception to the Greenland Ice Sheet, is consistent between PlioMIP1 and PlioMIP2. The implementation of dynamic global vegetation models by PlioMIP2 participant groups will allow investigation of the sensitivity of ESS/CS to vegetation-climate feedbacks. We also recognise that CS and ESS calculations are model dependent and this will be looked at in detail in the multi-model comparison of PlioMIP2 results. Precipitation change is more complex. Pliocene geography is the primary driver of geographical distribution changes in precipitation, whilst both Pliocene geography and CO_2 increase the globally integrated MAP.

We find an AMOC which is more intense in the Pliocene than in the pre-industrial, the variation driven principally by the change in geography (Table 7). We determine this by comparing AMOC strength of E^{280} against Eoi^{400} and Eoi^{280}. In addition we have explored the sensitivity of AMOC strength to methodology applied for fresh water correction. The Eoi^{280} experiment uses a fixed fresh water correction field corresponding to pre-industrial iceberg trajectories whilst the Pliocene experiment uses an annually-derived correction (Section 2.2), in theory this could impact on simulated AMOC intensity in Eoi^{400} versus E^{280}. To test this we have conducted an additional E^{280} experiment using the annually-derived fresh water correction methodology of Eoi^{400} (results not shown). This has demonstrated for the pre-industrial that the fresh water correction method does not lead to a statistically different AMOC strength. This indicates that our intensified AMOC within Eoi^{400} is indeed a consequence of palaeogeographic changes, rather than our approach to fresh water correction.

Both the choice of TSI (1361 vs. 1365 Wm⁻²) and PRISM4 orbital configuration (modern vs. 3.205 Ma) have been shown not to significantly influence the anomaly-type analysis in use by the Pliocene community. For example we show that the representation of the KM5c (3.205 Ma) time slice with a modern orbit is an acceptable choice - leading to no statistically significant differences within MASAT (Table 3) or MAP (Table 4) which is in accordance with previous work (Haywood et al., 2013a). When considering absolute values or climatic indices the influence of TSI or orbit is minimal but should nevertheless be considered. Models with greater climate sensitivity will present more sensitivity to TSI and potential for non-linearities in climate response (e.g. relating to feedbacks at or near the sea-ice edge or climate-vegetation interactions).

Whilst the Pliocene represents an incredibly useful contemporary-climate analogue, the use of a non-modern palaeogeography (enhanced PRISM4 boundary condition dataset) does present limitations when using low to intermediate spatial resolution

30　climate models. Regridding of the LSM to the 3.75°×2.5° model is imperfect due to the binary nature of the data and therefore requires manual corrections driven by an understanding of model architecture and physics (i.e. imposed by rigid-lid streamfunction, horizontal grid-type etc.). As a pre-cursor, some *a priori* knowledge of important aspects of Pliocene ocean circulation is required to guide a series of expert-informed decisions on model configuration. Similarly, when model development teams (e.g. MOHC) create present-day boundary conditions, knowledge of circulation patterns and throughflow strength is often used to

35　inform manual corrections (e.g artificial deepening of narrow channels) or the inclusion of parametrisations (e.g. diffusive pipes to represent otherwise unrepresented, narrow straits). This *a priori* knowledge is not necessarily available for the Pliocene and it is therefore difficult to assess. An example of this is in the subaerial extension of Ireland and Scotland within PRISM4 and how this is represented within the model and how this may influence the Norwegian Current. Additionally, the use of different model architectures and models with higher spatial resolution within the PlioMIP2 framework may allow these aspects to be

5　considered. For example, free-surface ocean models with higher horizontal spatial resolution may help in the interpretation of the Pliocene ACC strength and the Pliocene Arctic Ocean cold anomaly identified within this study.

　　Palaeogeographic induced changes in mean state, for example the path of the Antarctic Coastal Current around the Peninsula island (Section 4.2.5) represent non-analogous characteristics imposed by the PRISM4 Pliocene reconstruction. Other potentially non-analogous changes are associated with palaeogeographical changes to the Maritime continent and subsequent

10　changes in Indonesian throughflow configuration, the closure of the Bering Strait and Canadian Archipelago, and the withdrawal of the Baltic Sea and Hudson Bay. These palaeogeographical changes should be considered alongside those described within Hill (2015) such as the suggestion of extensive uplift in the Barents Sea (e.g. Knies et al. (2014)) and the rerouting of major rivers (e.g. within North American) which may be currently unrepresented within the model. These important regional changes must be considered when considering the KM5c time slice as an equilibrium state analogue to contemporary climate

15　change (i.e. a 400 ppm world).

References

Archer, C. L. and Caldeira, K.: Historical trends in the jet streams, Geophysical Research Letters, 35, https://doi.org/10.1029/2008GL033614, 2008.

Bonham, S. G., Haywood, A. M., Lunt, D. J., Collins, M., and Salzmann, U.: El Niño Southern Oscillation, Pliocene climate and equifinality, Philosophical Transactions of the Royal Society A: Mathematical, Physical and Engineering Sciences, 367, 127–156, https://doi.org/10.1098/rsta.2008.0212, 2009.

Braconnot, P., Otto-Bliesner, B., Harrison, S., Joussaume, S., Peterchmitt, J.-Y., Abe-Ouchi, A., Crucifix, M., Driesschaert, E., Fichefet, T., Hewitt, C. D., Kageyama, M., Kitoh, A., Laîné, A., Loutre, M.-F., Marti, O., Merkel, U., Ramstein, G., Valdes, P., Weber, S. L., Yu, Y., and Zhao, Y.: Results of PMIP2 coupled simulations of the Mid-Holocene and Last Glacial Maximum - Part 1: experiments and large-scale features, Climate of the Past, 3, 261–277, https://doi.org/10.5194/cp-3-261-2007, https://www.clim-past.net/3/261/2007/, 2007.

Bragg, F. J., Lunt, D. J., and Haywood, A. M.: Mid-Pliocene climate modelled using the UK Hadley Centre Model: PlioMIP Experiments 1 and 2, Geoscientific Model Development, 5, 1109–1125, https://doi.org/10.5194/gmd-5-1109-2012, 2012.

Bryan, K.: Climate and the Ocean Circulation, Monthly Weather Review, 97, 806–827, 1969.

Bryan, K., Manabe, S., and Packanowski, R. C.: A global ocean-atmosphere climate model. II the oceanic circulation, Journal of Physical Oceanography, 5, 30–46, https://doi.org/10.1175/1520-0485(1975)005<0030:AGOACM>2.0.CO;2, 1975.

Burls, N. J., Fedorov, A. V., Sigman, D. M., Jaccard, S. L., Tiedemann, R., and Haug, G. H.: Active Pacific meridional overturning circulation (PMOC) during the warm Pliocene, Science Advances, 3, https://doi.org/10.1126/sciadv.1700156, 2017.

Chandan, D. and Peltier, W. R.: Regional and global climate for the mid-Pliocene using the University of Toronto version of CCSM4 and PlioMIP2 boundary conditions, Climate of the Past, 13, 919–942, https://doi.org/10.5194/cp-13-919-2017, https://www.clim-past.net/13/919/2017/, 2017.

Chandler, M. A., Sohl, L. E., Jonas, J. A., Dowsett, H. J., and Kelley, M.: Simulations of the mid-Pliocene Warm Period using two versions of the NASA/GISS ModelE2-R Coupled Model, Geosci. Model Dev., 6, 517–531, https://doi.org/10.5194/gmd-6-517-2013, 2013.

Cox, M.: A Primitive Equation, 3-dimensional Model of the Ocean, GFDL Ocean Group technical report, Geophysical Fluid Dynamics Laboratory/NOAA, Princeton University, 1984.

Cox, P. M., Betts, R. A., Bunton, C. B., Essery, R. L. H., Rowntree, P. R., and Smith, J.: The impact of new land surface physics on the GCM simulation of climate and climate sensitivity, Climate Dynamics, 15, 183–203, https://doi.org/10.1007/s003820050276, 1999.

Cunningham, S. A., Alderson, S. G., King, B. A., and Brandon, M. A.: Transport and variability of the Antarctic Circumpolar Current in Drake Passage, Journal of Geophysical Research: Oceans, 108, https://doi.org/10.1029/2001JC001147, 2003.

Cusack, S., Slingo, A., Edwards, J. M., and Wild, M.: The radiative impact of a simple aerosol climatology on the Hadley Centre atmospheric GCM, Quarterly Journal of the Royal Meteorological Society, 124, 2517–2526, https://doi.org/10.1002/qj.49712455117, 1998.

Dolan, A. M., Haywood, A. M., Hill, D. J., Dowsett, H. J., Hunter, S. J., Lunt, D. J., and Pickering, S. J.: Sensitivity of Pliocene ice sheets to orbital forcing, Palaeogeography, Palaeoclimatology, Palaeoecology, 309, 98–110, https://doi.org/10.1016/j.palaeo.2011.03.030, 2011.

Dowsett, H., Dolan, A., Rowley, D., Moucha, R., Forte, A. M., Mitrovica, J. X., Pound, M., Salzmann, U., Robinson, M., Chandler, M., Foley, K., and Haywood, A.: The PRISM4 (mid-Piacenzian) paleoenvironmental reconstruction, Climate of the Past, 12, 1519–1538, https://doi.org/10.5194/cp-12-1519-2016, 2016.

Dowsett, H. J., Foley, K. M., Stoll, D. K., Chandler, M. A., Sohl, L. E., Bentsen, M., Otto-Bliesner, B. L., Bragg, F. J., Chan, W.-L., Contoux, C., Dolan, A. M., Haywood, A. M., Jonas, J. A., Jost, A., Kamae, Y., Lohmann, G., Lunt, D. J., Nisancioglu, K. H., Abe-

19

Ouchi, A., Ramstein, G., Riesselman, C. R., Robinson, M. M., Rosenbloom, N. A., Salzmann, U., Stepanek, C., Strother, S. L., Ueda, H., Yan, Q., and Zhang, Z.: Sea Surface Temperature of the mid-Piacenzian Ocean: A Data-Model Comparison, Scientific Reports, 3, 1–8, https://doi.org/10.1038/srep02013, 2013.

15 Edwards, M. O.: Global gridded elevation and bathymetry on 5-minute geographic grid (ETOPO5), in: Data Announcement 88-MGG-02, Digital relief of the Surface of the Earth, Boulder, Colorado, 1989.

Essery, R. L. H., Best, M. J., Best, R. A., Cox, P. M., and Taylor, C. M.: Explicit Representation of Subgrid Heterogeneity in a GCM Land Surface Scheme, Journal of Hydrometeorology, pp. 530–543, https://doi.org/10.1175/1525- 7541(2003)004<0530:EROSHI>2.0.CO;2, 2003.

20 Good, P., Jones, C., Lowe, J., Betts, R., and Gedney, N.: Comparing Tropical Forest Projections from Two Generations of Hadley Centre Earth System Models, HadGEM2-ES and HadCM3LC, Journal of Climate, 26, 495–511, https://doi.org/10.1175/JCLI-D-11-00366.1, 2013.

Gordon, A. L. and Fine, R. A.: Pathways of water between the Pacific and Indian oceans in the Indonesian seas, Nature, 379, 146–149, https://doi.org/10.1038/379146a0, 1996.

25 Gordon, C., Cooper, C., Senior, C. A., Banks, H., Gregory, J. M., Johns, T. C., Mitchell, J. F. B., and Wood, R. A.: The simulation of SST, sea ice extents and ocean heat transports in a version of the Hadley Centre coupled model without flux adjustments, Climate Dynamics, 16, 147–168, https://doi.org/10.1007/s003820050010, 2000.

Griesel, A., Mazloff, M. R., and Gille, S. T.: Mean dynamic topography in the Southern Ocean: Evaluating Antarctic Circumpolar Current transport, Journal of Geophysical Research: Oceans, 117, https://doi.org/10.1029/2011JC007573, 2012.

30 Haywood, A. M., Dolan, A. M., Pickering, S. J., Dowsett, H. J., McClymont, E. L., Prescott, C. L., Salzmann, U., Hill, D. J., Hunter, S. J., Lunt, D. J., Pope, J. O., and Valdes, P. J.: On the identification of a Pliocene time slice for data-model comparison, Philosophical Transactions of the Royal Society A: Mathematical, Physical and Engineering Sciences, 371, https://doi.org/10.1098/rsta.2012.0515, 2013a.

Haywood, A. M., Hill, D. J., Dolan, A. M., Otto-Bliesner, B. L., Bragg, F., Chan, W.-L., Chandler, M. A., Contoux, C., Dowsett, H. J.,
35 Jost, A., Kamae, Y., Lohmann, G., Lunt, D. J., Abe-Ouchi, A., Pickering, S. J., Ramstein, G., Rosenbloom, N. A., Salzmann, U., Sohl, L., Stepanek, C., Ueda, H., Yan, Q., and Zhang, Z.: Large-scale features of Pliocene climate: results from the Pliocene Model Intercomparison Project, Climate of the Past, 9, 191–209, https://doi.org/10.5194/cp-9-191-2013, https://www.clim-past.net/9/191/2013/, 2013b.

Haywood, A. M., Dowsett, H. J., Dolan, A. M., Rowley, D., Abe-Ouchi, A., Otto-Bliesner, B., Chandler, M. A., Hunter, S. J., Lunt, D. J., Pound, M., and Salzmann, U.: The Pliocene Model Intercomparison Project (PlioMIP) Phase 2: scientific objectives and experimental design, Climate of the Past, 12, 663–675, https://doi.org/10.5194/cp-12-663-2016, 2016.

5 Hibler, W. D.: A Dynamic Thermodynamic Sea Ice Model, Journal of Physical Oceanography, 9, 815–846, https://doi.org/10.1175/1520-0485(1979)009<0815:ADTSIM>2.0.CO;2, 1979.

Hill, D. J.: The non-analogue nature of Pliocene temperature gradients, Earth and Planetary Science Letters, 425, 232–241, https://doi.org/https://doi.org/10.1016/j.epsl.2015.05.044, 2015.

Howell, F. W., Haywood, A. M., Dolan, A. M., Dowsett, H. J., Francis, J. E., Hill, D. J., Pickering, S. J., Pope, J. O., Salzmann, U., and Wade,
10 B. S.: Can uncertainties in sea ice albedo reconcile patterns of data-model discord for the Pliocene and 20th/21st centuries?, Geophysical Research Letters, 41, 2011–2018, https://doi.org/10.1002/2013GL058872, 2014.

Johns, T. C., Gregory, J. M., Ingram, W. J., Johnson, C. E., Jones, A., Lowe, J. A., Mitchell, J. F. B., Roberts, D. L., Sexton, D. M. H., Stevenson, D. S., Tett, S. F. B., and Woodage, M. J.: Anthropogenic climate change for 1860 to 2100 simulated with the HadCM3 model under updated emissions scenarios., Climate Dynamics, 20, 583–612, https://doi.org/10.1007/s00382-002-0296-y, 2003.

15 Kamae, Y., Yoshida, K., and Ueda, H.: Sensitivity of Pliocene climate simulations in MRI-CGCM2.3 to respective boundary conditions, Climate of the Past, 12, 1619–1634, https://doi.org/10.5194/cp-12-1619-2016, https://www.clim-past.net/12/1619/2016/, 2016.

Knies, J., Mattingsdal, R., Fabian, K., Grøsfjeld, K., Baranwal, S., Husum, K., Schepper, S. D., Vogt, C., Andersen, N., Matthiessen, J., Andreassen, K., Jokat, W., Nam, S.-I., and Gaina, C.: Effect of early Pliocene uplift on late Pliocene cooling in the Arctic-Atlantic gateway, Earth and Planetary Science Letters, 387, 132–144, https://doi.org/https://doi.org/10.1016/j.epsl.2013.11.007, 2014.

20 Koch, P., Wernli, H., and Davies, H. C.: An event-based jet-stream climatology and typology, International Journal of Climatology, 26, 283–301, https://doi.org/10.1002/joc.1255, 2006.

Kopp, G. and Lean, J. L.: A new, lower value of total solar irradiance: Evidence and climate significance, Geophysical Research Letters, 38, 5–48, https://doi.org/10.1029/2010GL045777, 2011.

Levitus, S. and Boyer, T. P.: World Ocean Atlas, p. 117pp, https://repository.library.noaa.gov/view/noaa/1381, 1994.

25 Li, D. and Shine, K. P.: A 4-Dimensional Ozone Climatology for UGAMP Models, UGAMP Internal Report No. 35, http://catalogue.ceda.ac.uk/uuid/bff84b935ce5aa9f04624777b0eea507, 1995.

LSCE: PMIP2 Boundary Conditions, https://pmip2.lsce.ipsl.fr/design/boundary.shtml, accessed: 14-04-2019, 2007.

Lunt, D. J., Valdes, P. J., Haywood, A., and Rutt, I. C.: Closure of the Panama Seaway during the Pliocene: implications for climate and Northern Hemisphere glaciation, Climate Dynamics, 30, 1–18, https://doi.org/10.1007/s00382-007-0265-6, 2008.

30 Matthes, K., Funke, B., Andersson, M. E., Barnard, L., Beer, J., Charbonneau, P., Clilverd, M. A., Dudok de Wit, T., Haberreiter, M., Hendry, A., Jackman, C. H., Kretzschmar, M., Kruschke, T., Kunze, M., Langematz, U., Marsh, D. R., Maycock, A. C., Misios, S., Rodger, C. J., Scaife, A. A., Seppälä, A., Shangguan, M., Sinnhuber, M., Tourpali, K., Usoskin, I., van de Kamp, M., Verronen, P. T., and Versick, S.: Solar forcing for CMIP6 (v3.2), Geoscientific Model Development, 10, 2247–2302, https://doi.org/10.5194/gmd-10-2247-2017, 2017.

McCarthy, G. D., Smeed, D. A., Johns, W. E., Frajka-Williams, E., Moat, B. I., Rayner, D., Baringer, M. O., Meinen, C. S., Collins, 35 J., and Bryden, H. L.: Measuring the Atlantic Meridional Overturning Circulation at 26°N, Progress in Oceanography, 130, 91–111, https://doi.org/10.1016/j.pocean.2014.10.006, 2015.

Meftah, M., Dewitte, S., Irbah, A., Chevalier, A., Conscience, C., Crommelynck, D., Janssen, E., and Mekaoui, S.: SOVAP/Picard, a Space-borne Radiometer to Measure the Total Solar Irradiance, Solar Physics, 289, 1885–1899, https://doi.org/10.1007/s11207-013-0443-0, 2014.

Meijers, A. J. S., Shuckburgh, E., Bruneau, N., Sallee, J.-B., Bracegirdle, T. J., and Wang, Z.: Representation of the Antarctic Circumpolar 5 Current in the CMIP5 climate models and future changes under warming scenarios, Journal of Geophysical Research: Oceans, 117, https://doi.org/10.1029/2012JC008412, 2012.

NCAS: Computational Modelling Services. Tools and Utilities, http://cms.ncas.ac.uk/wiki/ToolsAndUtilities, accessed: 14-04-2019, 2019.

Pardaens, A. K., Banks, H. T., Gregory, J. M., and Rowntree, P. R.: Freshwater transports in HadCM3, Climate Dynamics, 21, 177–195, https://doi.org/10.1007/s00382-003-0324-6, 2003.

10 Pope, V. D., Gallani, M. L., Rowntree, P. R., and Stratton, R. A.: The impact of new physical parametrizations in the Hadley Centre climate model: HadAM3, Climate Dynamics, 16, 123–146, https://doi.org/10.1007/s003820050009, 2000.

Prescott, C. L., Haywood, A. M., Dolan, A. M., Hunter, S. J., Pope, J. O., and Pickering, S. J.: Assessing orbitally-forced interglacial climate variability during the mid-Pliocene Warm Period, Earth and Planetary Science Letters, 400, 261–271, https://doi.org/https://doi.org/10.1016/j.epsl.2014.05.030, 2014.

15 Randall, D., Wood, R., Bony, S., Colman, R., Fichefet, T., Fyfe, J., Kattsov, V., Pitman, A., Shukla, J., Srinivasan, J., Ronald, S., Sumi, A., and Taylor, K.: Climate Models and Their Evaluation, pp. 589–662, Cambridge University Press, Cambridge, United Kingdom and New York, NY, USA, 2007.

Roether, W., Roussenov, V. M., and Well, R.: A Tracer Study of the Thermohaline Circulation of the Eastern Mediterranean, pp. 371–394, Springer Netherlands, Dordrecht, https://doi.org/10.1007/978-94-011-0870-6_16, 1994.

20 Semtner, A. J.: A model for the thermodynamic growth of sea ice in numerical investigations of climate, Journal of Physical Oceanography, 6, 379–389, https://doi.org/10.1175/1520-0485(1976)006<0379:AMFTTG>2.0.CO;2, 1976.

Stachnik, J. P. and Schumacher, C.: A comparison of the Hadley circulation in modern reanalyses, Journal of Geophysical Research: Atmospheres, 116, https://doi.org/10.1029/2011JD016677, 2011.

Taylor, K. E., Stouffer, R. J., and Meehl, G. A.: An Overview of CMIP5 and the Experiment Design, Bulletin of the American Meteorological
25 Society, 93, 485–498, https://doi.org/10.1175/BAMS-D-11-00094.1, 2012.

Tindall, J. C. and Haywood, A. M.: Modeling oxygen isotopes in the Pliocene: Large-scale features over the land and ocean, Paleoceanography, 30, 1183–1201, https://doi.org/10.1002/2014PA002774, 2015.

Tribe, A.: Automated recognition of valley lines and drainage networks from grid digital elevation models: a review and a new method, Journal of Hydrology, pp. 263–293, https://doi.org/10.1016/0022-1694(92)90206-B, 1992.

30 USGS: Pliocene Model Intercomparison Project, Phase 2, https://geology.er.usgs.gov/egpsc/prism/7_pliomip2.html, accessed: 14-04-2019, 2016.

USGS: PMIP2 Model Data List, https://geology.er.usgs.gov/egpsc/prism/data/PlioMIP2_Model_Data_List_updated2018.htm, accessed: 14-04-2019, 2018.

Valdes, P. J., Armstrong, E., Badger, M. P. S., Bradshaw, C. D., Bragg, F., Crucifix, M., Davies-Barnard, T., Day, J. J., Farnsworth, A., Gordon, C., Hopcroft, P. O., Kennedy, A. T., Lord, N. S., Lunt, D. J., Marzocchi, A., Parry, L. M., Pope, V., Roberts, W. H. G., Stone, E. J., Tourte, G. J. L., and Williams, J. H. T.: The BRIDGE HadCM3 family of climate models: HadCM3@Bristol v1.0, Geoscientific Model
680 Development, 10, 3715–3743, https://doi.org/10.5194/gmd-10-3715-2017, 2017.

Wilson, M. and Henderson-Sellers, A.: A global archive of land cover and soils data for use in General Circulation Climate Models, Journal of Climatology, 5, 119–143, https://doi.org/10.1002/joc.3370050202, 1985.

Zhang, Z.-S., Nisancioglu, K. H., Chandler, M. A., Haywood, A. M., Otto-Bliesner, B. L., Ramstein, G., Stepanek, C., Abe-Ouchi, A., Chan, W.-L., Bragg, F. J., Contoux, C., Dolan, A. M., Hill, D. J., Jost, A., Kamae, Y., Lohmann, G., Lunt, D. J., Rosenbloom, N. A., Sohl,
685 L. E., and Ueda, H.: Mid-pliocene Atlantic Meridional Overturning Circulation not unlike modern, Climate of the Past, 9, 1495–1504, https://doi.org/10.5194/cp-9-1495-2013, 2013.
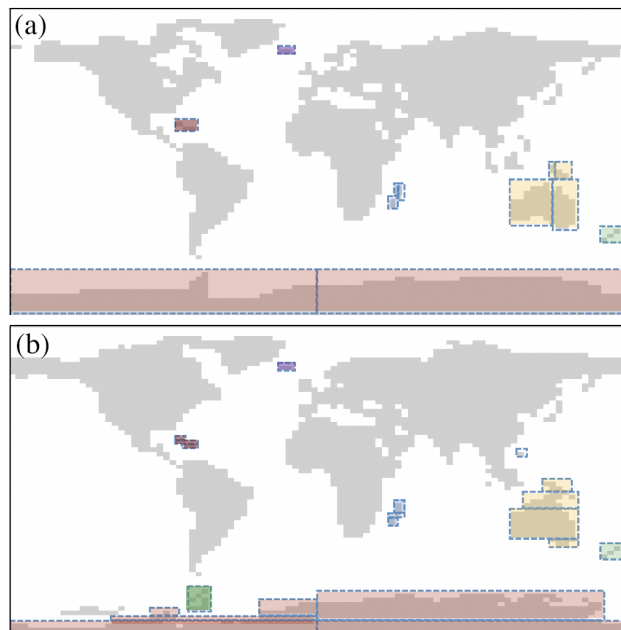
**Figure 1.** LSM and barotropic streamfunction island configuration for the (a) pre-industrial and (b) Pliocene.
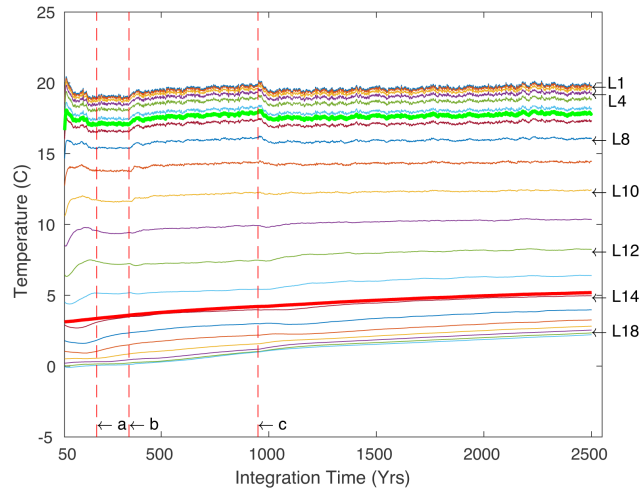
Figure 2. Time-evolution of the globally-integrated temperature for the ocean layers within the Eoi[400] experiment. Whole ocean volume indicated by the thick red line and the top 200 m indicated by the thick green line. Vertical lines indicate key spin-up stages; (a) adding the barotropic physics to the ocean model, (b) incorporation of barotropic streamfunction islands into the barotropic solver, and (c) correction to the barotropic streamfunction island in the southern high-latitudes and incorporation of full PRISM4 vegetation boundary conditions into the model. The mid points to the ocean layers are 5 m (L1), 15 m (L2), 15 m (L3), 35 m (L4), 48 m (L5), 67 m (L6), 96 m (L7), 139 m (L8), 204 m (L9), 301 m (L10), 447 m (L11), 666 m (L12), 996 m (L13), 1501 m (L14), 2116 m (L15), 2731 m (L16), 3347 m (L17), 3962 m (L18), 4577 m (L19) and 5195 m (L20).
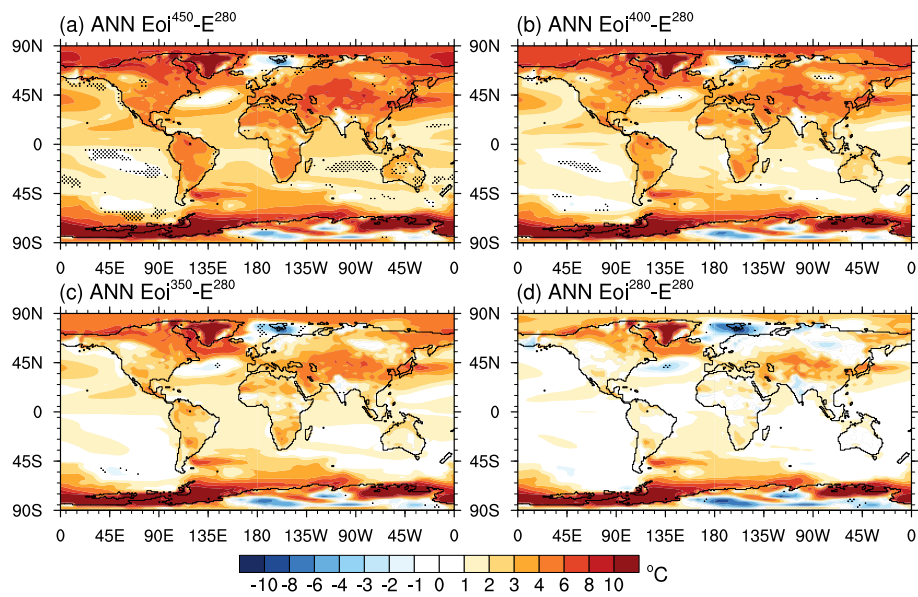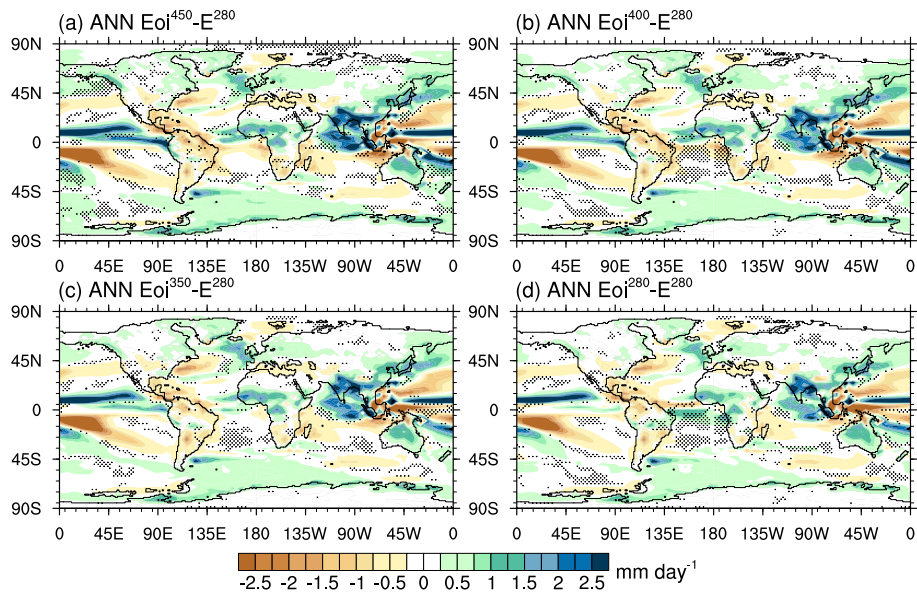
Figure 3. Pliocene annual mean surface air temperature anomalies against E^{280}. (a) $Eoi^{450}-E^{280}$, (b) $Eoi^{400}-E^{280}$, (c) $Eoi^{350}-E^{280}$ and (d) $Eoi^{280}-E^{280}$. Stippling indicates regions in which results are not statistically significant at a 95% confidence criteria (independent two-sample Student t-test).
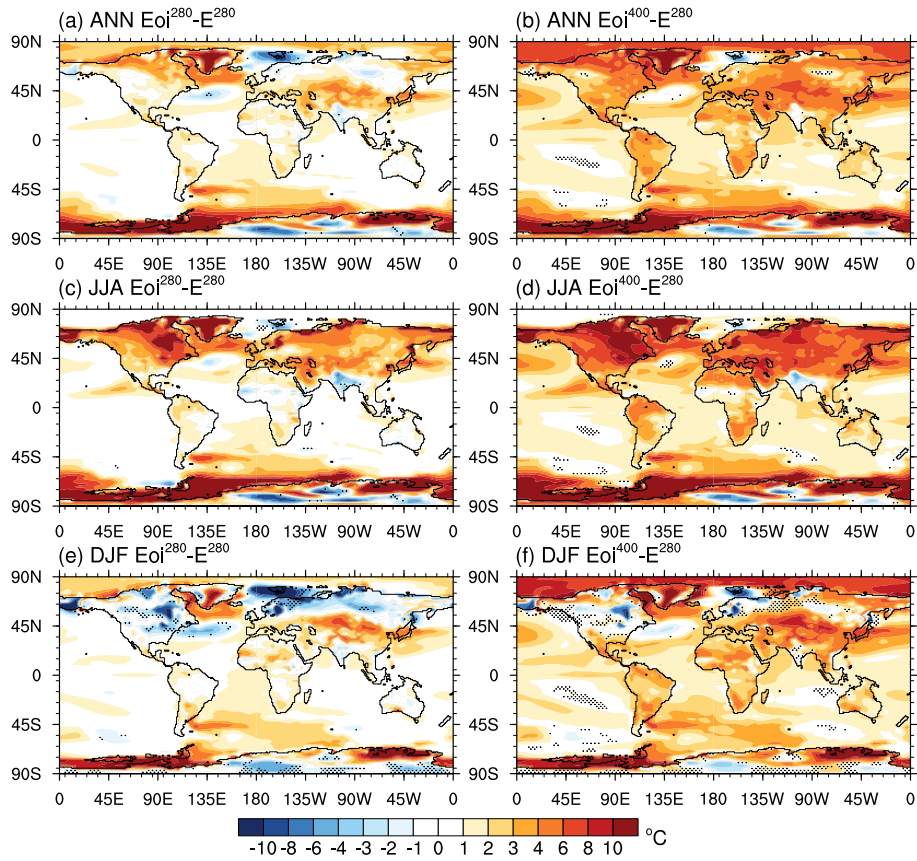
Figure 4. Mean annual and seasonal Pliocene temperature anomalies against E^{280}. (a) Annual Eoi^{280}-E^{280}, (b) Annual Eoi^{400}-E^{280}, (c) June-July-August (JJA) Eoi^{280}-E^{280}, (d) JJA Eoi^{400}-E^{280}, (e) December-January-February (DJF) Eoi^{280}-E^{280} and (f) DJF Eoi^{400}-E^{280}. Stippling indicates regions in which results are not statistically significant at a 95% confidence criteria.
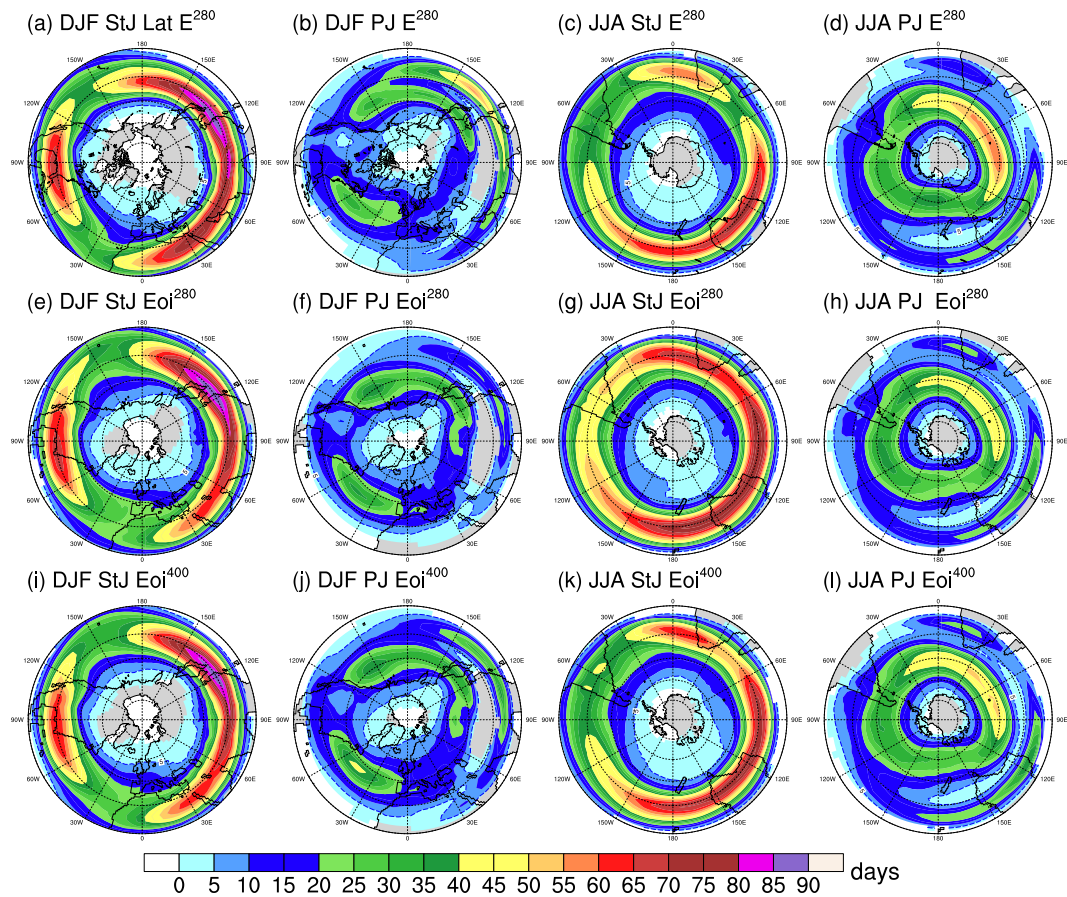
Figure 5. Pliocene mean annual precipitation anomalies against E^{280}. (a) Eoi^{450}-E^{280}, (b) Eoi^{400}-E^{280}, (c) Eoi^{350}-E^{280} and (d) Eoi^{280}-E^{280}. Stippling indicates regions in which results are not statistically significant at a 95% confidence criteria.
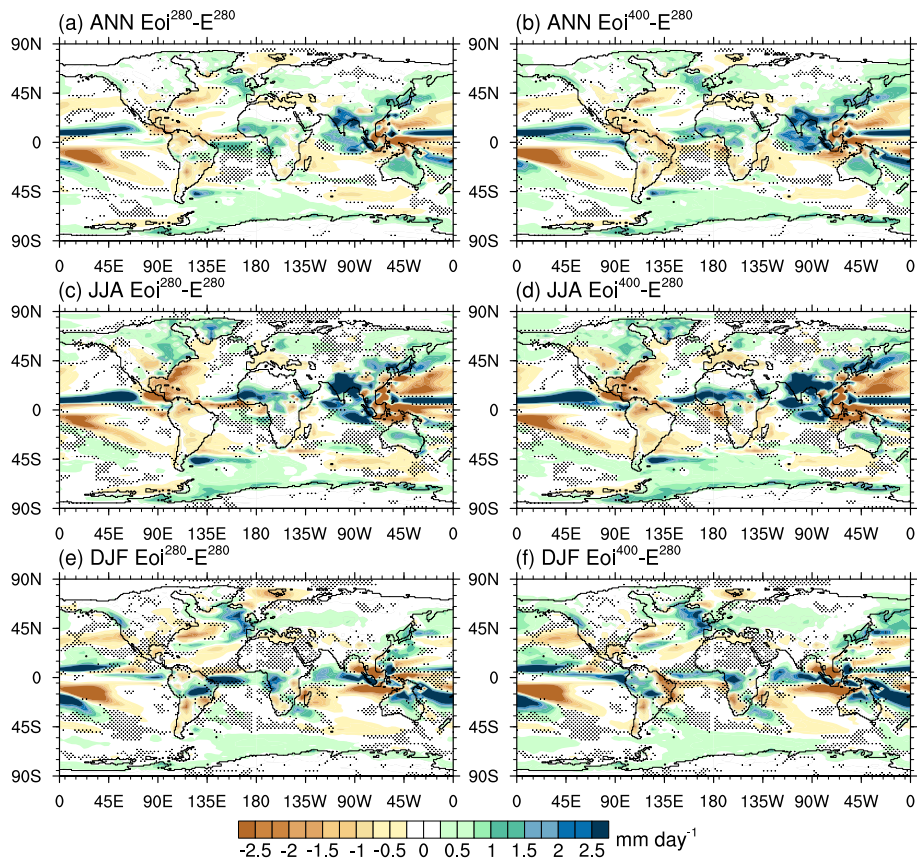
Figure 6. Mean Annual and seasonal Pliocene precipitation anomalies. (a) Annual Eoi[280]-E[280], (b) Annual Eoi[400]-E[280], (c) JJA Eoi[280]-E[280], (d) JJA Eoi[400]-E[280], (e) DJF Eoi[280]-E[280] and (f) DJF Eoi[400]-E[280]. Stippling indicates regions in which results are not statistically significant at a 95% confidence criteria.
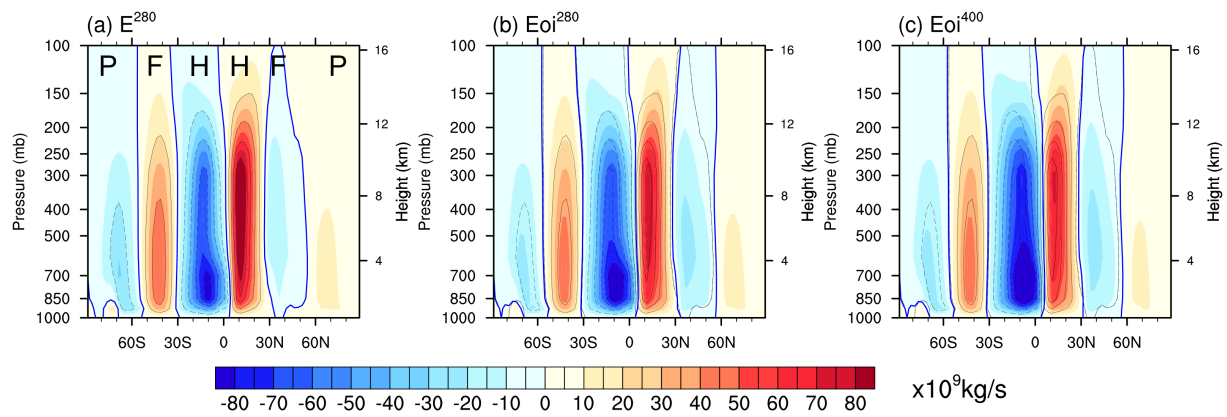
Figure 7. Mean annual zonally-averaged meridional mass stream function for (a) E ^{280}, (b) Eoi^{280} and (c) E^{400}. The contour lines are from E^{280} and are shown for intervals of 2×10^{10} kg s^{-1} with dashed lines indicating counterclockwise (looking westward) circulation (ascending air moves southward). The solid blue contour indicates zero meridional streamfunction indicative of the boundary of circulation cells. The Hadley (H), Ferrel (F) and the Polar (P) cells are indicated within (a).

Figure 8. Seasonal (DJF and JJA) distribution of the Subtropical Jet (StJ) and Polar Jet streams (PJ) for (a-d) E [280], (e-h) Eoi[280], and (i-l) E[400]. Colour scale indicates mean number of days within season in which wind speed $>$30 ms^{-1} over 400 - 100 hPa. Note that the wind-shear PJ classification identifies a jet downstream of the Himalayas.
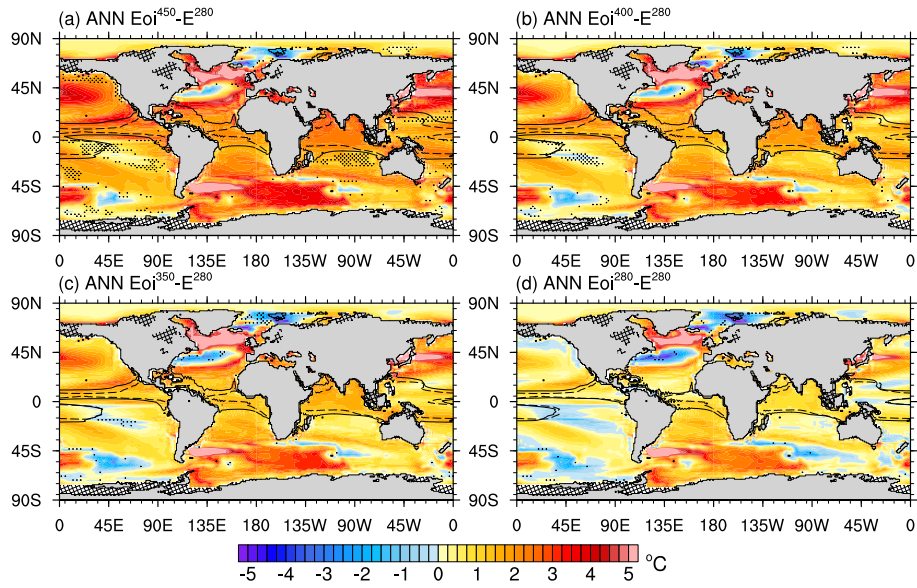
Figure 9. Pliocene mean annual sea surface temperature (MASST) anomalies against E^{280}. (a) Eoi^{450}-E^{280}, (b) Eoi^{400}-E^{280}, (c) Eoi^{350}-E^{280} and (d) Eoi^{280}-E^{280}. Dotted contour lines indicates E^{280} 28°C warm pool whilst the solid contour indicates the Pliocene 28°C warm pool. Cross hatching indicates regions in which either modern or Pliocene have contrasting land surface. Stippling indicates regions in which there is no statistical difference at a 95% confidence criteria.
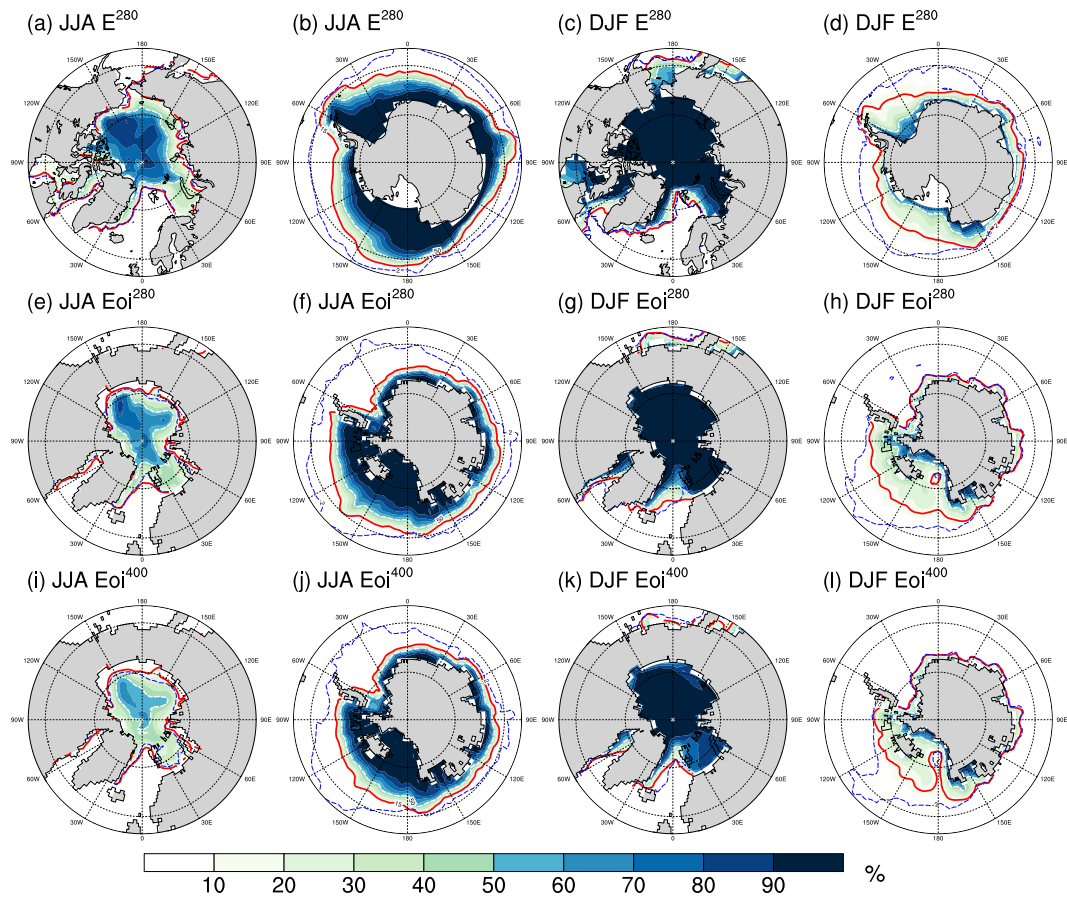
**Figure 10.** Sea ice concentrations (%) during JJA and DJF in the Northern and Southern hemisphere for (a-d) E^{280}, (e-h) Eoi^{280}, and (i-l) Eoi^{400}. The red line indicates the sea ice edge based on a threshold of 15% whilst the dotted white line indicates the 50% threshold. The blue dotted line indicates the 2°C isotherm, in the Southern Ocean this is indicative of the Antarctic convergence zone (polar front).
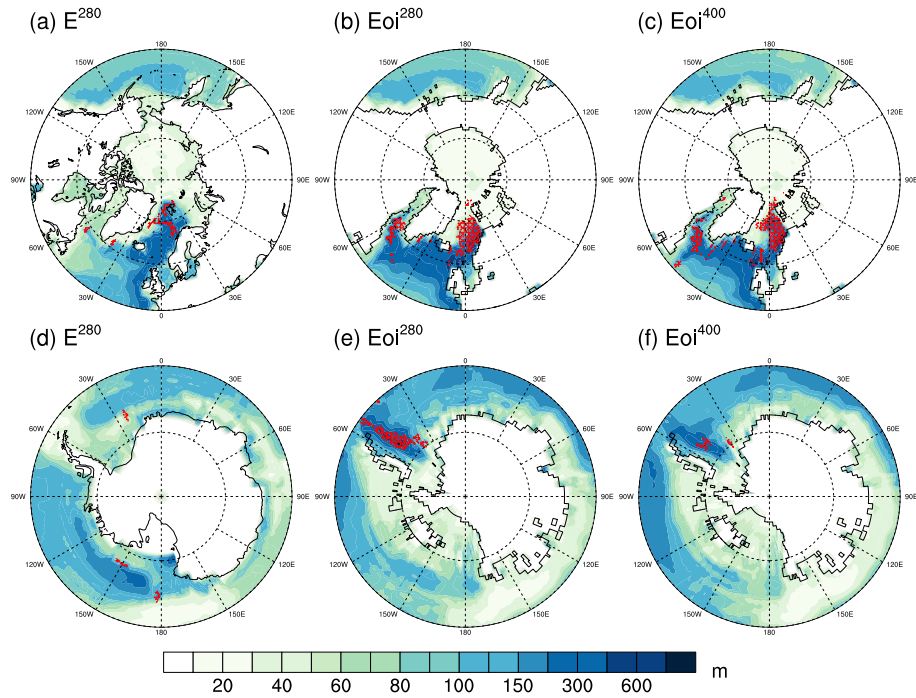
Figure 11. Mean March Northern Hemisphere and September Southern Hemisphere Mixed Layer Depth for (a and d) E^{280}, (b and e) Eoi^{280} and (c and f) Eoi^{400}. Red hashes indicate regions that exhibit deep (>1000 m) convection at least 1 month during the climatologcal meaning period, single-cell ocean regions have been expanded slightly to improve visualisation.
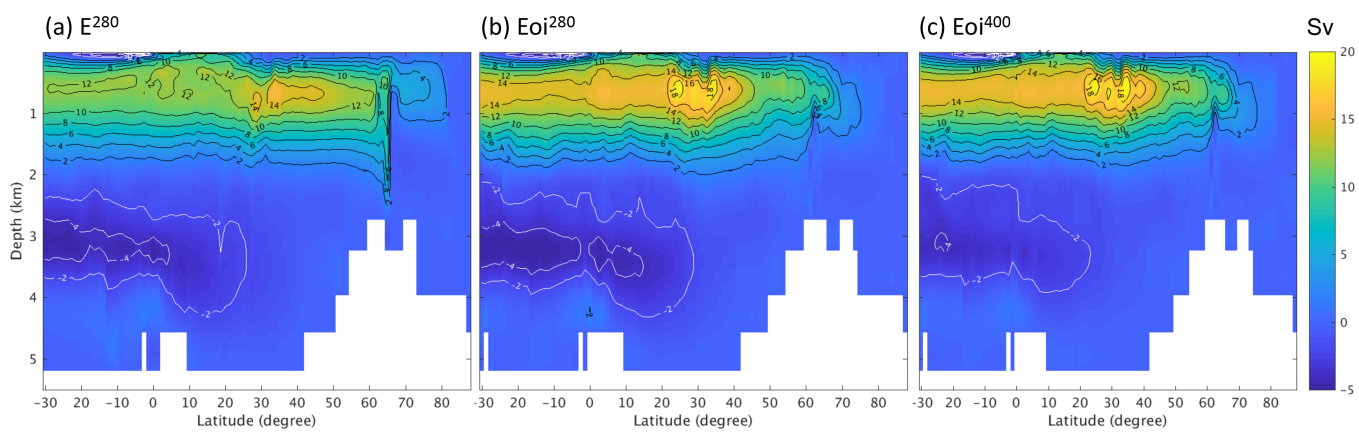
Figure 12. Time-averaged Atlantic overturning circulation for (a) E^{280}, (b) Eoi^{280} and (c) Eoi^{400}. Positive values indicate clockwise circulation.
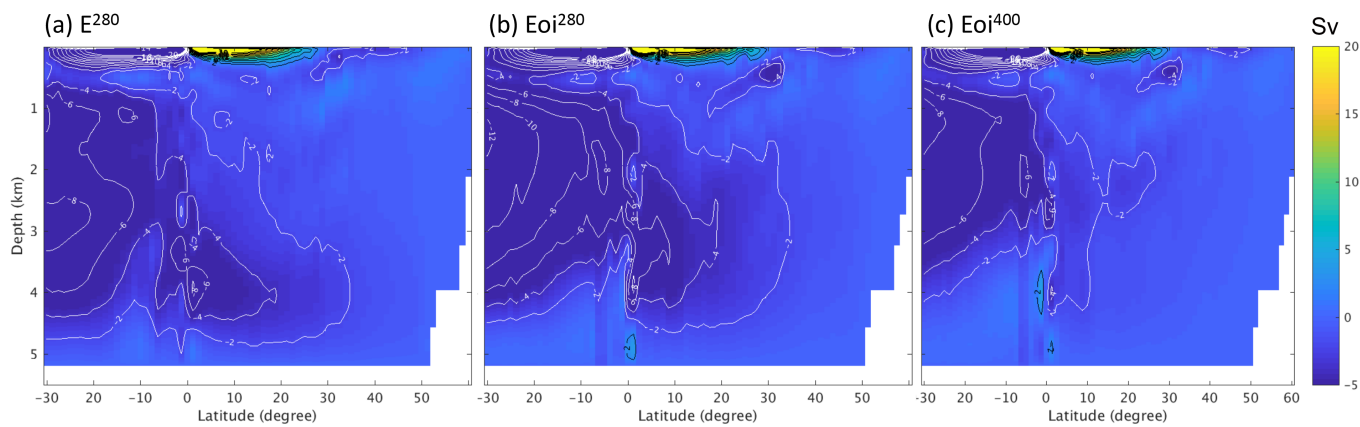
Figure 13. Time-averaged Pacific overturning circulation for (a) E^{280}, (b) Eoi^{280} and (c) Eoi^{400}. Positive values indicate clockwise circulation.
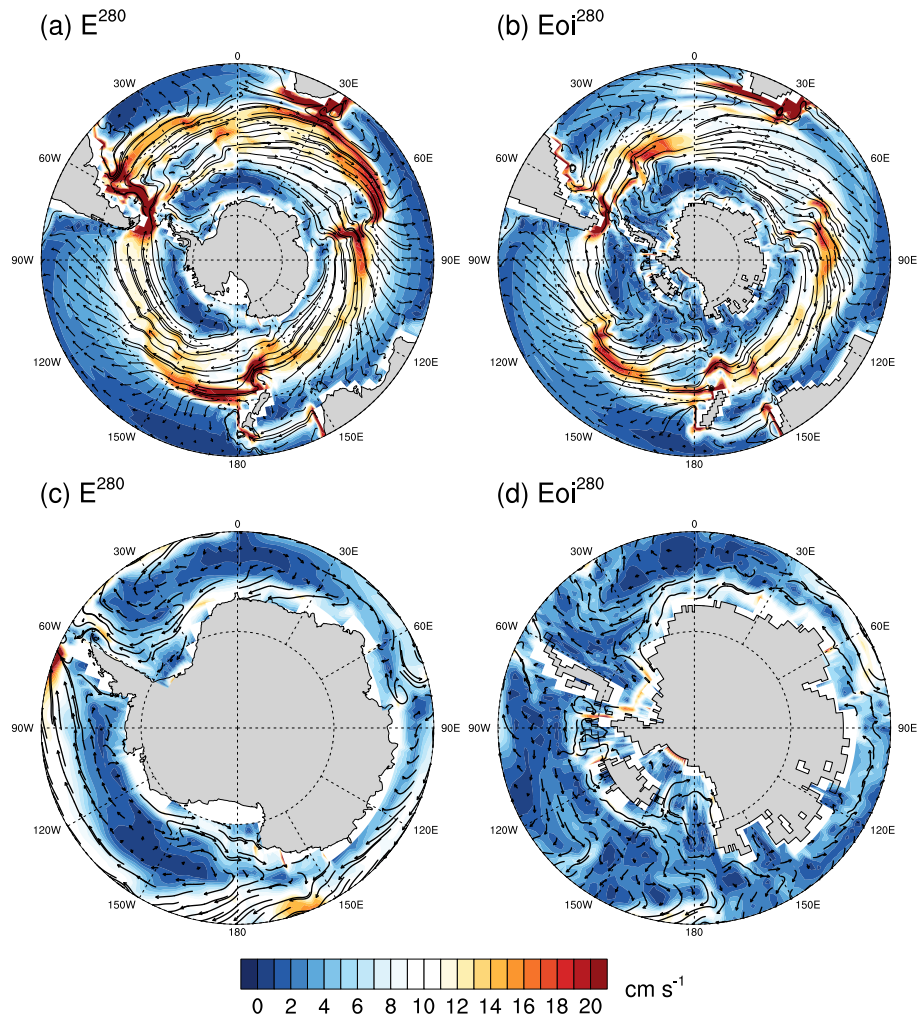
Figure 14. Surface ocean mean annual velocity (streamlines and vector magnitude) for E^{280} and Eoi^{280}. The ACC is shown clearly within (a) E^{280} and (b) Eoi^{280}, whilst the Antarctic Coastal Current is shown within the close-up plots (c) E^{280} and (d) Eoi^{280}.
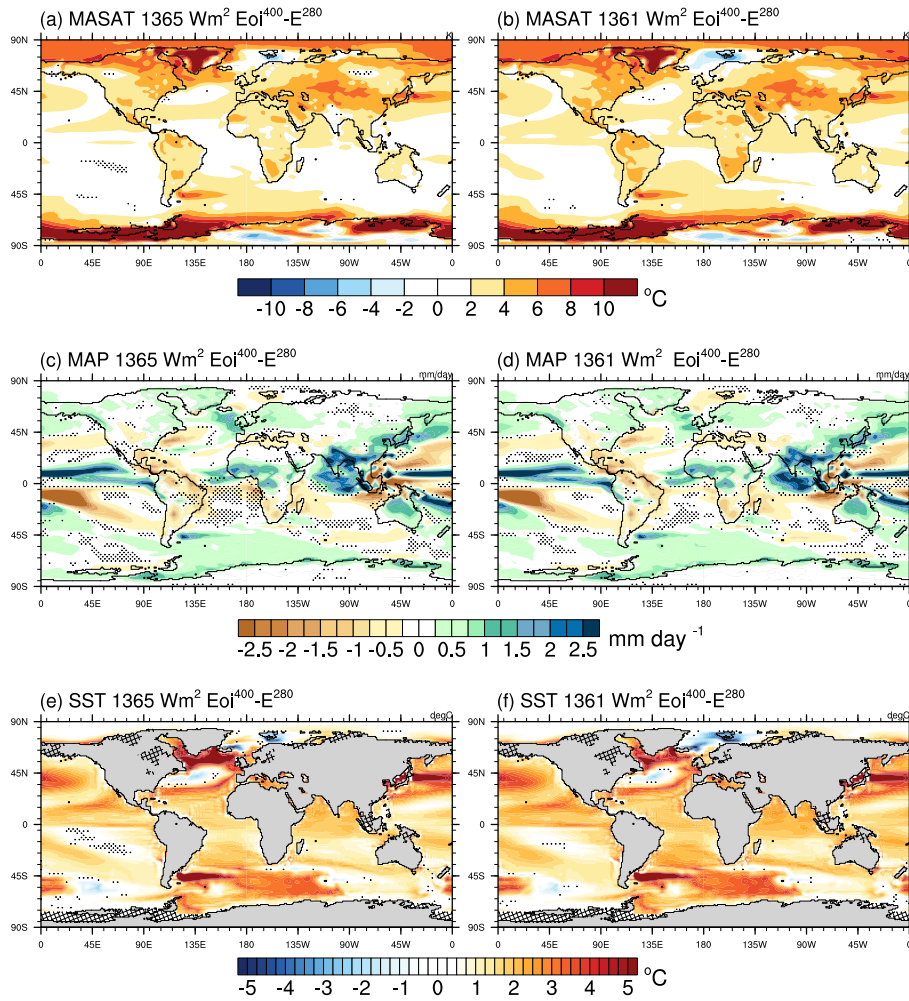
Figure 15. Sensitivity of Eoi[400] -E[280] anomalies on TSI values for (a and b) MASAT, (c and d) MAP, and (e and f) MASST.

Table 1. Summary of simulations conducted within this study. Those in italic represent simulations beyond the PlioMIP2 experiment design.

N°/	ID	Geography	PlioMIP2 component	Description
1	Eoi^{400}	Pliocene	CORE	Full enhanced boundary conditions with fixed vegetation and 400 ppm CO_2
2	Eoi^{450}	Pliocene	T1 P4F & P4P	As Eoi^{400} but with 450 ppm CO_2
3	Eoi^{350}	Pliocene	T1 P4F & P4P	As Eoi^{400} but with 350 ppm CO_2
4	Eoi^{280}	Pliocene	T2 P4F & P4P	As Eoi^{400} but with 280 ppm CO_2
5	E^{280}	PI	CORE	Standard pre-industrial boundary conditions with fixed vegegation and 280 ppm CO_2
6	E^{400}	PI	T2 P4F & P4P	As E^{280} but with 400 ppm CO_2
7	E^{560}	PI	T1 P4F	As E^{280} but with 560 ppm CO_2
8	$_{orb}Eoi^{400}$	Pliocene	Additional sensitivity	As of Eoi^{400} but with 3.205 Ma orbit (KM5c)
9	$_{1361}Eoi^{400}$	Pliocene	Additional sensitivity	As Eoi^{400} but with TSI=1361 Wm^{-2}
10	$_{1361}E^{280}$	PI	Additional sensitivity	As E^{280} but with TSI=1361 Wm^{-2}

The following definitions are used: pre-industrial (PI), Tier 1 (T1), Tier 2 (T2), Pliocene for Future (P4F), Pliocene for Pliocene (P4P) and Total Solar Irradiance (TSI).

Table 2. Summary of equilibrium state parameters for the seven PlioMIP2 protocol experiments. Globally integrated ($Ocean_{all}$) and surface Ocean (top 200m; $Ocean_{surf}$) climatological trends and Top of the Atmosphere Energy Balance (TOA_{EB}) are derived from the last 100 model years.

ID	$Ocean_{all}$ (°C $cent^{-1}$)	$Ocean_{surf}$ (°C $cent^{-1}$)	TOA_{EB} (Wm^{-2})
Eoi^{450}	0.063	0.046	0.260
Eoi^{400}	0.041	-0.026	0.047
Eoi^{350}	0.017	0.002	-0.024
Eoi^{280}	0.017	0.002	-0.090
E^{280}	-0.014	0.008	-0.115
E^{400}	-0.048	0.010	0.098
E^{560}	0.107	0.025	0.334

Table 3. Global mean annual surface air temperature (MASAT) decomposed into polar (poleward of 60°) and tropical (equaterward of 30°) regions. The Polar amplification factor is shown in square brackets and is defined as the *ratio* in the anomalies (against E^{280}) between the polar warming and the global mean warming.

ID	MASAT (°C)	△ T against E^{280}	North Pole MASAT (°C)	tropical MASAT (°C)	South Pole MASAT (°C)
Eoi^{450}	17.4 ± 0.1	+3.4	-4.6 ± 0.4 [1.6]	27.6 ± 0.1	-10.5 ± 0.4 [2.1]
Eoi^{400}	16.9 ± 0.1	+2.9	-5.2 ± 0.3 [1.7]	27.2 ± 0.1	-11.2 ± 0.3 [2.2]
$_{orb}$Eoi^{400}	16.8 ± 0.1	+2.8	-5.2 ± 0.4 [1.7]	27.1± 0.1	-11.4 ± 0.3 [2.2]
Eoi^{350}	16.3 ± 0.1	+2.3	-6.2± 0.3 [1.7]	26.7 ± 0.2	-11.8 ± 0.4 [2.5]
Eoi^{280}	15.4 ± 0.1	+1.4	-8.1 ± 0.4 [1.4]	25.9 ± 0.1	-12.6 ± 0.3 [3.5]
E^{280}	14.0 ± 0.1	0	-10.0 ± 0.3	25.1 ± 0.2	-17.5 ± 0.3
E^{400}	15.8 ± 0.1	+1.8	-6.8 ± 0.3 [1.8]	26.5 ± 0.2	-15.5 ± 0.4 [1.1]
E^{560}	17.5 ± 0.1	+3.5	-3.8 ± 0.3 [1.8]	28.0 ± 0.2	-13.4 ± 0.4 [1.2]

Table 4. Globally integrated mean annual precipitation (MAP).

ID	MAP (mm day^{-1})
Eoi^{450}	3.041 ± 0.007
Eoi^{400}	3.025 ± 0.008
$_{orb}$Eoi^{400}	3.027 ± 0.008
Eoi^{350}	3.012 ± 0.009
Eoi^{280}	2.979 ± 0.008
E^{280}	2.912 ± 0.008
E^{400}	2.975 ± 0.007
E^{560}	3.019 ± 0.008

Table 5. Integrated mean core latitude of the Subtropical Jet (StJ) for E^{280}, Eoi^{280} and Eoi^{400} experiments during December-January-February (DJF) and June-July-August (JJA) seasons. Note that only the StJ is reported as it more stable and persistent than the Polar Jet.

ID	NH DJF (°N)	NH JJA (°N)	SH DJF (°S)	SH JJA (°S)
Eoi^{400}	32.8 ± 1.5	47.0 ± 2.4	44.8 ± 1.9	33.9 ± 1.3
Eoi^{280}	32.0 ± 1.1	46.2 ± 1.9	44.7 ± 1.8	33.7 ± 1.5
E^{280}	30.3 ± 1.4	44.6 ± 3.0	42.5 ± 1.3	33.5 ± 1.8

Table 6. Global mean annual sea surface temperature (MASST) and defining characteristics of the equatorial warm pool regions.

ID	MASST (°C)	GWP ($\times 10^6$ km^2)	WHWP$_{max}$ ($\times 10^6$ km^2)	IPWP$_{max}$ [year-round] ($\times 10^6$ km^2)
Eoi^{450}	20.3 ± 0.1	107.5 ± 2.5	25.2 ± 0.6	95.7 ± 2.8 [63.0 ± 2.8]
Eoi^{400}	19.9 ± 0.1	99.7 ± 2.6	24.4 ± 0.5	89.0 ± 3.3 [57.1 ± 2.1]
$_{orb}$Eoi^{400}	19.8 ± 0.1	98.5 ± 2.8	23.8 ± 0.5	87.4 ± 3.0 [56.2 ± 1.9]
Eoi^{350}	19.6 ± 0.1	92.1 ± 3.1	23.1 ± 0.5	82.4 ± 3.7 [50.9 ± 2.6]
Eoi^{280}	18.9 ± 0.1	78.8 ± 2.9	19.7 ± 1.2	71.7 ± 3.0 [38.6 ± 3.3]
E^{280}	18.1 ± 0.1	66.4 ± 4.5	15.0 ± 1.5	62.8 ± 3.9 [25.4 ± 3.1]
E^{400}	19.3 ± 0.1	91.5 ± 3.3	22.1 ± 1.3	85.6 ± 3.9 [50.8 ± 3.2]
E^{560}	20.4 ± 0.1	117.2 ± 3.3	27.2 ± 1.5	102.9 ± 2.5 [68.9 ± 2.6]

The Global Warm Pool (GWP) area defined using Mean Annual Sea Surface Temperature (MASST) and a 28°C. Western Hemisphere Warm Pool (WHWP; 130°W - 45°W), Indo-Pacific Warm Pool (IPWP; 30° E - 60°W) are defined as the max monthly mean area that is 28°C. For IPWP$_{max}$ the number in parenthesis is the area that is 28°C year-round.

Table 7. Characteristics of the Atlantic and Pacific Meridional Overturning Circulation (AMOC and PMOC).

ID	AMOC$_{max}$ (Sv)	AMOC$_{max}$ 26.5°N (Sv)	PMOC$_{+ve}$ (Sv)	PMOC$_{-ve}$ (Sv) [Depth (m)] PDW ($\geq$30°S below 500 m)
Eoi^{450}	18.6 ± 1.1	16.3 ± 1.0	39.3 ± 4.0	-9.3 ± 1.5 [1000]
Eoi^{400}	19.6 ± 1.0	17.2 ± 0.8	40.6 ± 3.0	-9.1 ± 1.4 [1000]
$_{orb}$Eoi^{400}	21.4 ± 1.5	19.3 ± 1.1	40.9 ± 3.3	-9.8 ± 1.9 [1000]
Eoi^{350}	20.4 ± 1.1	18.8 ± 0.9	42.2 ± 3.9	-9.8 ± 1.8 [1000]
Eoi^{280}	18.9 ± 0.8	17.4 ± 0.9	46.0 ± 3.4	-12.3 ± 1.6 [1500]
E^{280}	15.7 ± 1.2	13.4 ± 1.1	33.4 ± 3.1	-8.6 ± 1.4 [2700]
E^{400}	15.2 ± 1.2	13.6 ± 1.0	29.3 ± 2.5	-9.0 ± 0.9 [3960]
E^{560}	15.9 ± 1.3	13.8 ± 0.9	25.0 ± 2.1	7.6 ± 0.8 [3960]

AMOC$_{max}$ is the maximum AMOC. PMOC$_{+ve}$ reflects the subtropical gyre circulation whilst PMOC$_{-ve}$ reflects the Pacific Deep Water (PDW) and North Pacific Deep Water (NPDW).

Table 8. Characteristics of the Antarctic Circumpolar Current (ACC) within the Pliocene and pre-industrial experiments. From the barotropic streamfunction we derive the mean ACC latitude (the Polar front) from the centroid of the zonal transport and the core width derived from the $\pm$ 50% boundary.

ID	ACC at 65°W (Sv)	Mean ACC latitude (°S)	Mean ACC core width (°)
Eoi^{450}	78.3 ± 2.9	58.8	11.5
Eoi^{400}	76.7 ± 2.8	58.8	11.8
$_{\text{orb}}\text{Eoi}^{400}$	77.3 ± 2.9	58.7	11.8
Eoi^{350}	73.5 ± 3.0	58.8	11.9
Eoi^{280}	51.6 ± 31.9	60.0	12.6
E^{280}	179.0 ± 11.2	66.0	33.6
E^{400}	186.6 ± 9.0	66.6	33.3

Table 9. Sensitivity of E^{280} and Eoi^{400} (and their corresponding anomalies) to TSI of 1361 and 1365 Wm^{-2}. Shown are the mean annual surface air temperature (MASAT), mean annual precipitation (MAP), mean annual sea surface temperature (MASST), Atlantic and Pacific meridional circulation (AMOC_{max} and $\text{PMOC}_{+ve,-ve}$; Section 4.2.4), and Antarctic Circumpolar Current (ACC; Section 4.2.5).

ID	MASAT (°C)	MAP (mm day^{-1})	MASST (°C)	AMOC_{max} (Sv)	$\text{PMOC}_{+ve,-ve}$ (Sv)	ACC (Sv)
E^{280}	14.0 ± 0.1	2.912 ± 0.008	18.1 ± 0.1	15.7 ± 1.2	$33.4 \pm 3.1, -8.6 \pm 1.4$	179.0 ± 11.1
$_{1361}\text{E}^{280}$	13.7 ± 0.1	2.885 ± 0.008	17.9 ± 0.1	16.3 ± 1.2	$33.8 \pm 3.9, -9.2 \pm 1.5$	180.0 ± 6.2
Eoi^{400}	16.9 ± 0.1	3.025 ± 0.008	19.9 ± 0.1	19.6 ± 1.0	$40.6 \pm 3.0, -9.1 \pm 1.4$	76.7 ± 2.8
$_{1361}\text{Eoi}^{400}$	16.7 ± 0.1	3.014 ± 0.010	19.7 ± 0.1	17.0 ± 0.9	$37.7 \pm 3.3, -8.5 \pm 1.7$	76.0 ± 2.5
$\text{Eoi}^{400}\text{-E}^{280}$	2.9 ± 0.1	0.113 ± 0.011	1.8 ± 0.1	3.9 ± 1.6	$7.2 \pm 4.3, -0.5 \pm 2.0$	-102.3 ± 11.4
$_{1361}\text{Eoi}^{400}\text{-}_{1361}\text{E}^{280}$	3.0 ± 0.1	0.129 ± 0.013	1.8 ± 0.1	0.7 ± 1.5	$3.9 \pm 5.1, 0.7 \pm 1.3$	-104.0 ± 6.7